

Nelson et al.

Highlights

- Tissue insulin action was driven by gene-by-environment interactions
- Adipose insulin resistance was dissociated from systemic insulin resistance
- Large adipocytes were strongly tied with adipose insulin resistance
- Muscle insulin resistance was linked with hyperinsulinemia and decreased glycolysis

eTOC blurb

This investigation of mouse strains by Nelson et al. revealed that muscle insulin resistance was most closely linked to levels of circulating insulin and muscle glycolytic enzymes. Intriguingly, certain strains had enlarged fat cells and adipose insulin resistance, but completely healthy muscle insulin response, showing tissue-specific progression toward metabolic disease.

Systems level analysis of insulin action in mouse strains provides insight into tissue and pathway specific interactions that drive insulin resistance

AUTHORS: Marin E. Nelson^{1,2,*}, Søren Madsen^{1,2,*}, Kristen C. Cooke^{1,2,*}, Andreas M. Fritzen^{1,2}, Ida H. Thorius^{1,2}, Stewart W. C. Masson^{1,2}, Luke Carroll^{1,2}, Fiona C. Weiss^{1,2}, Marcus M. Seldin³, Meg Potter^{1,2}, Samantha L. Hocking^{2,4}, Daniel J. Fazakerley^{1,2}, Amanda E. Brandon^{2,4}, Senthil Thillainadesan^{1,2}, Alistair M. Senior^{1,2}, Gregory J. Cooney^{2,4}, Jacqueline Stöckli^{1,2} and David E. James^{1,2,4,#}

¹School of Life and Environmental Sciences, University of Sydney, Camperdown, New South Wales, 2006, Australia

²Charles Perkins Centre, University of Sydney, Camperdown, New South Wales 2006, Australia

³Department of Biological Chemistry and Center for Epigenetics and Metabolism, University of California, Irvine, CA, 92697, USA

⁴Faculty of Medicine and Health, University of Sydney, Camperdown, New South Wales, 2006, Australia

* These authors contributed equally to this work

Lead contact (#): David James. Address: D17 - Charles Perkins Centre, University of Sydney, Camperdown, New South Wales, 2006, Australia. Phone: +61 2 8627 1621.

Email: david.james@sydney.edu.au

SUMMARY

Skeletal muscle and adipose tissue insulin resistance are major drivers of metabolic disease. To uncover pathways involved in insulin resistance specifically in these tissues, we leveraged the metabolic diversity of different dietary exposures and discrete inbred mouse strains. This revealed that muscle insulin resistance was driven by gene-by-environment interactions and was strongly correlated with hyperinsulinemia and decreased levels of ten key glycolytic enzymes. Remarkably, there was no relationship between muscle and adipose tissue insulin action. Adipocyte size profoundly varied across strains and diets, and this was strongly correlated with adipose tissue insulin resistance. The A/J strain in particular exhibited marked adipocyte insulin resistance and hypertrophy despite robust muscle insulin responsiveness, challenging the role of adipocyte hypertrophy *per se* in systemic insulin resistance. These data demonstrate that muscle and adipose tissue insulin resistance can occur independently and underscore the need for tissue-specific interrogation to understand metabolic disease.

KEY WORDS

Insulin resistance; skeletal muscle; adipose; metabolism; glucose uptake; GxE; Western diet; glycolysis

INTRODUCTION

Insulin resistance (IR) is the catalyst for multiple metabolic diseases including type 2 diabetes (T2D), dyslipidemia and coronary artery disease (DeFronzo and Tripathy, 2009; Hanley et al., 2002; Lillioja et al., 1993). Because skeletal muscle is considered the primary site of insulin-stimulated glucose disposal in the body, IR in this tissue is considered to be a major contributor to disease progression (DeFronzo and Tripathy, 2009) yet the principal drivers of muscle IR remain unclear in part because studies examining muscle insulin action in humans and mice often use surrogate measures (James et al., 2021).

Recent data implicate an important role for tissue crosstalk via several models: 1) insulin resistant adipose tissue (AT) changes its secretory profile including lipid factors (Abel et al., 2001), adipokines such as leptin and adiponectin, or inflammatory cytokines (Gancheva et al., 2018; Indrakusuma et al., 2015; da Silva Rosa et al., 2020) to alter whole-body insulin sensitivity; 2) limited capacity of the adipocyte to store lipid leads to lipid spillover and ectopic lipid deposition in other tissues including muscle, leading to IR (Jo et al., 2009; Kim et al., 2000; Rodeheffer et al., 2008); 3) the expansion of existing fat cells or hypertrophy is often associated with poor metabolic outcomes while fat cell hyperplasia is accompanied by a more metabolically healthy phenotype (Kim et al., 2015; Vishvanath and Gupta, 2019). Other factors such as hyperinsulinemia have also been postulated to play a major role in muscle IR (Del Prato et al., 1994; Iozzo et al., 2001; Koopmans et al., 1997), but because hyperinsulinemia co-exists with IR, it has been difficult to experimentally disentangle its role in the pathogenesis of metabolic diseases.

One difficulty in studying IR is that IR risk is heightened by a complex interplay of genetic and environmental factors. Yet most studies only interrogate one of these parameters without taking account of the other. For example, in human studies it is difficult to quantify or accurately control the environment (Tam et al., 2019) while most animal studies, where it is relatively simple to control the environment, tend to overlook the contribution of genetics. This concept was well-illustrated in a study that measured IR-related traits across the Hybrid Mouse Diversity Panel (HMDP), a repository of genetically diverse inbred mouse strains (Parks et al., 2015). This study revealed a 63-fold difference across mouse strains in HOMA-IR (homeostasis model assessment of IR), a surrogate measure of IR that does not resolve tissue-specific IR. Other studies that included genetically diverse strains combined multiple layers of omics in livers from the BXD or HMDP mouse reference populations with QTL analysis identifying several genetic variants controlling transcription through metabolite levels and, ultimately, liver-specific traits (Parker et al., 2019; Williams et al., 2016). However, a detailed analysis of skeletal muscle and white AT insulin action across a diverse panel of inbred mice is lacking. In the current study, we utilized the diversity in metabolic responses observed across different mouse strains exposed to two different diets to capture the heritability of metabolic traits, and the effect of diet and strain-by-diet interactions, to unravel aspects of metabolic disease. This approach uncoupled muscle and AT insulin responsiveness, with muscle but not AT being associated with systemic insulin sensitivity. Although large adipocytes were associated with AT insulin resistance, this was not the case for muscle IR, challenging the view that large adipocytes are metabolically deleterious. Finally, proteomic analysis of soleus muscle revealed a decline in the levels of both mitochondrial and glycolytic enzymes in IR indicating an overall decline in substrate

utilization in muscle insulin resistance, rather than a switch away from mitochondrial oxidation toward glycolysis.

RESULTS

Characterization of diverse inbred mouse strains

We selected thirteen inbred mouse strains from the HMDP and the ILSXISS lines that displayed varying degrees of metabolic dysfunction (Parks et al., 2015; Stöckli et al., 2017) and exposed them to either chow or high-fat high-sucrose Western diet (WD) for 8 wks. We next measured a range of metabolic and morphometric parameters (for strain abbreviations, see STAR Methods). While most strains were quite similar when fed chow diet, there were exceptions, with DBA and BALB exhibiting greater adiposity and AKR were more glucose intolerant than many other strains. Even more diversity was observed in response to WD. For example, WD-fed BXH9, DBA and BL/6 displayed all the hallmarks of diet-induced metabolic disease including high adiposity, hyperglycemia, hyperinsulinemia and glucose intolerance, while A/J and BALB developed neither hyperinsulinemia nor glucose intolerance, despite gaining considerable adiposity when fed WD (**Fig. 1A-D, Fig. S1A-I**), as previously shown (Montgomery et al., 2013; Surwit et al., 1988). NOD maintained normal fasting glucose when fed WD but developed glucose intolerance. ILSX97 developed marked obesity but relatively mild changes in other parameters, while BXD34 remained lean and did not display any features of the metabolic syndrome when fed WD. These data highlight the

variability in insulin action and metabolic homeostasis between different inbred mouse strains.

Tissue insulin responsiveness

For subsequent in-depth analysis of insulin action in AT and muscle, we selected seven of the thirteen strains, which covered the full physiological spectrum of metabolic phenotypes on WD, with BL/6 representing the most commonly-used reference strain. BXH9 displayed significant glucose intolerance, hyperinsulinemia and hyperglycemia on WD compared to chow. BXD34 was refractory to many effects of WD including excess adiposity, glucose intolerance and hyperinsulinemia. A/J and BALB showed no difference in many metabolic parameters on WD compared to chow (glucose tolerance, fasting insulin, insulin AUC, fasting glucose) despite similar adiposity as BL/6 on WD and were hence selected as the “metabolically healthy obese” group. 129 and ILSX97 were intermediate, as on WD they displayed a trend towards hyperinsulinemia: 129 was glucose intolerant and both strains were obese, with ILSX97 showing the largest fold increase in adiposity on WD of any strain. We studied tissue-specific insulin action of soleus and extensor digitorum longus (EDL), as these represent red and white muscles, respectively. In addition, we studied epididymal AT, as it is highly metabolically responsive and secretes a range of factors that can impact muscle metabolism (Li et al., 2020). We measured glucose uptake as this represents the major insulin-regulated process in these tissues that is defective in IR. We used a maximal insulin dose (10 nM) to achieve a robust measure of insulin responsiveness, as muscle insulin action is defective in IR even at a maximal dose (James et al., 2021; Kolterman et al., 1980). We

observed robust increases in glucose uptake in response to a maximum insulin dose in soleus, EDL and AT explants by as much as four-fold (**Fig. 2A-F; Fig. S2A-C**). Soleus and EDL differed markedly in their response to diet (**Fig 2A-B**). Insulin-stimulated glucose uptake (GU:I) into soleus was significantly impaired by WD in all strains except for A/J (**Fig. 2A**), whereas EDL was resistant to WD effects except in the case of BXH9 (**Fig. 2B**). AT GU:I also varied considerably between strains under chow conditions, but these strain differences collapsed to similar levels with WD (**Fig. 2C**). Chow-fed BL/6, BALB and BXD34 had robust responses in terms of AT GU:I, and WD feeding significantly impaired these responses (**Fig. 2C**). We also observed divergent patterns between muscle and AT GU:I between strains. For example, muscle from A/J mice was extremely insulin responsive even in WD-fed mice, but AT from these mice had a poor insulin response even under chow-fed conditions. This highlights the important contribution of muscle, but not AT, to whole-body glucose homeostasis. Conversely, chow-fed BL/6 had the lowest rates of GU:I into soleus or EDL, but among the highest rates into AT. There was minimal variation in basal glucose uptake across strains and diets for all three tissues (**Fig. S2A-C**).

Adipocyte cell size

Adipocytes can expand either via hypertrophy or hyperplasia in response to a positive energy balance, and adipocyte hypertrophy is often associated with poor metabolic outcomes (Kim et al., 2015). There was considerable diversity in adipocyte size among the different strains even in chow-fed mice, exemplified by an interquartile range (IQR) of 528 μm^2 in chow-fed ILSX97 compared to 1654 μm^2 in chow-fed A/J. Adipocytes from chow-fed ILSX97 were the smallest with the lowest IQR than other

strains, but demonstrated profound hypertrophy under WD conditions. Conversely, adipocytes of BXD34 mice showed little hypertrophy in response to WD, remaining the smallest of the WD-fed mice (**Fig. 3A-C**), consistent with the fact that these mice did not develop obesity in response to WD (**Fig 1A**). Strikingly, adipocytes from chow-fed A/J were larger with a greater IQR than the other strains fed the same diet and even larger than several WD-fed strains (**Fig 3A-C**). Both the median adipocyte size and the variability (IQR) in size was markedly increased by WD in most strains except BXD34. Consistent with previous studies in humans (Salans et al., 1968), we noticed an inverse relationship between adipocyte size and insulin action in AT. For example, A/J had the largest adipocytes and the lowest rate of AT GU:I of the chow-fed groups, whereas BXD34 had the smallest adipocytes and the highest rate of AT GU:I of the WD-fed groups (**Fig. 2C**).

To confirm the defect in AT glucose uptake in A/J mice (**Fig. 2C**), we measured glucose uptake into AT of chow-fed BL/6 and A/J mice *ex vivo*, across several insulin doses (**Fig. 3D**). This revealed a marked defect in AT glucose uptake in A/J mice at multiple insulin doses compared to BL/6 mice. We then investigated insulin signaling and the expression of the insulin responsive glucose transporter GLUT4, two main components of the insulin response pathway. Chow-fed A/J mice showed normal Akt phosphorylation compared to BL/6 as a reference (**Fig. 3E**) while GLUT4 protein levels were 65% lower in A/J (**Fig. 3F**) concomitant with decreased *Glut4* mRNA expression compared to BL/6 (**Fig. 3G**), which likely explains the lack of insulin response in A/J mice.

Influence of strain and environment on metabolic traits

To quantify strain, diet or strain-by-diet interactions on metabolic traits, we used linear mixed models to partition the variances of the traits into strain (broad sense heritability; H²), diet, and strain-by-diet (gene-by-environment; GxE) effects (**Fig. 4**). We were particularly interested in these effects on IR, as this has not been well-characterized. EDL GU:I had a relatively high H² (59%) with little diet contribution to the total variance (<1%), but substantial strain-by-diet interaction (21%). Soleus GU:I, on the other hand, had relatively low H² (26%) and strain-by-diet interaction (11%) compared to EDL, but a greater diet contribution to the total variance (17%). H² of AT GU:I was intermediate between that of EDL and soleus (42%), with similar strain-by-diet interaction as soleus (11%), but with less variance due to diet (8%). Thus, we observed different degrees of H² and diet responses of IR depending on the tissue. We expanded our survey to include other commonly-measured metabolic traits. Lean mass had the highest H² (76%) and negligible variance from diet (1%), whereas adiposity was the trait most affected by diet (47%). H² of fasting glucose was relatively high (50%), whereas diet or strain-by-diet interaction contributed little to the total variance of this trait (9% and 8%, respectively), as expected since most of our mice maintain well-regulated fasting glucose levels and did not show signs of overt diabetes despite WD feeding. In contrast, fasting insulin had lower H² (39%), but greater diet and strain-by-diet effects (33% and 12%, respectively). Importantly, we detected substantial GxE among the traits, such that diet had varying effects depending on the strain. This highlights the potential pitfalls of generalizing relationships between metabolic traits, or the effects of

metabolic interventions obtained from studies of a single inbred mouse strain to genetically diverse populations.

Clustering analysis of strains

To determine the relatedness of strains in terms of metabolic phenotypes, we z-scored measurements of tissue GU:I (**Fig. 2, Fig. S2**), related metabolic traits (**Fig. 1, Fig. S1**) and several surrogate measures of whole-body insulin sensitivity/resistance (**Fig. S3A-H**). Hierarchical clustering revealed that, overall, diet was a stronger driver of the phenotypic diversity between strains than strain *per se*, as diets tended to cluster together (**Fig. 5**). An exception to this was A/J chow, which fell within a cluster dominated by WD and was most closely related to A/J WD, largely driven by the low rates of GU:I into AT and the large adipocyte size. The other exception was BXD34 WD, which fell within the chow-dominated cluster and was most closely related to BL/6 chow and BXD34 chow. This is not surprising, as BXD34 were refractory to many effects of WD feeding (**Fig. 1**). The groups with the most severe metabolic disease profile (*i.e.* muscle IR, poor glucose tolerance, and hyperinsulinemia and HOMA-IR) with WD feeding were BXH9 and BL/6, and these groups clustered together such that they were distinct from all other groups based on these traits.

Metabolic trait correlations

Because of the lack of correspondence in insulin action between muscle and AT, we next aimed to identify tissue-specific indices of IR (**Fig. 6A**). As suspected, there

were no significant correlations between GU:I in AT and glucose uptake in either of the two muscles (soleus or EDL). The strongest correlates of Soleus GU:I were HOMA-IR, fasting plasma insulin and QUICKI ($R = -0.56, -0.53$ and 0.53 , respectively), which are commonly-used surrogate measures of whole-body insulin sensitivity. Interestingly, Soleus GU:I was also negatively correlated with epididymal and subcutaneous white AT mass (EpiWAT (g) and SCWAT (g); $R = -0.41$ and -0.40 , respectively), and to a lesser extent with adipocyte size ($R = -0.35$) and whole-body fat percentage (adiposity) ($R = -0.34$). Fasting insulin was the strongest correlate of EDL GU:I ($R = -0.35$). Soleus GU:I and EDL GU:I were weakly, but significantly, correlated ($R = 0.25$). Thus, despite differences in strain and diet effects between the two muscles, hyperinsulinemia was the systemic measure most strongly correlated with IR in both muscles. In the case of soleus, but not EDL, an index combining fasting plasma insulin and blood glucose (HOMA-IR) was more strongly correlated with IR than insulin alone. Interestingly, fasting glucose was significantly correlated with Soleus GU:I ($R = -0.45$) but not EDL GU:I, suggesting either that soleus glucose metabolism is more affected by exogenous glucose levels than EDL or, conversely, that glucose uptake into muscles with similar properties to soleus have a larger impact on fasting glucose levels than other muscle types.

In contrast to muscle, AT GU:I was not significantly correlated with hyperinsulinemia (**Fig. 6A**). Instead, the strongest correlates of adipose GU:I were overall adiposity and adipocyte size ($R = -0.48$ and -0.38 , respectively), whereas fat pad mass was not significantly correlated. Furthermore, adiposity was strongly correlated with adipocyte size ($R = 0.79$), suggesting adipocyte size (hypertrophy) was a stronger

driver of overall fat expansion with WD feeding than adipocyte proliferation (hyperplasia). The fact that adipocyte hypertrophy, but not fat pad mass, was significantly correlated with AT IR aligns with previous studies demonstrating that hypertrophy alone, rather than simply the expansion of fat pad mass due to a combination of adipocyte hypertrophy and hyperplasia, is more strongly associated with AT IR (Kim et al., 2015).

A network diagram of the traits which significantly correlated with GU:I in the muscles or AT (**Fig. 6B**) illustrates a striking difference between AT and Soleus GU:I in terms of network connectivity, each belonging to independent metabolic nodes. It is also apparent from this network that the commonly used *in vivo* measures, such as GTT and related indices (e.g. Matsuda index and IRI) were significantly correlated with Soleus GU:I, although not as strongly as fasting insulin and related indices (HOMA-IR and QUICKI) likely due to muscle-independent aspects of the GTT including glucose absorption by the gut, rates of secretion of paracrine hormones including insulin, and rates of liver glucose turnover (Bruce et al., 2021; Virtue and Vidal-Puig, 2021).

These correlations also highlight tissue-specific differences in insulin action. Soleus GU:I was correlated with a range of metabolic parameters commonly used as indicators of metabolic disease including hyperinsulinemia, hyperglycemia and obesity (fat %, fat pad weight and adipocyte size). In contrast, EDL GU:I was correlated with fasting insulin, but not with any measures of adiposity. The lack of correlation between EDL glucose uptake and most metabolic traits is not surprising, as diet had little impact on EDL insulin responsiveness. Despite a correlation between soleus insulin action and fat mass, there was no direct correlation between muscle and AT insulin action, making

it unlikely that changes in adipocyte insulin action, at least in the context of glucose uptake measured *ex vivo*, is a major driver of insulin action in muscle. Furthermore, this lack of direct correlation between muscle and AT action emphasizes the importance of tissue-specific analyses.

Soleus proteomics response networks

Because IR in muscle is a known precursor for metabolic diseases (DeFronzo and Tripathy, 2009; Hanley et al., 2002; Lillioja et al., 1993), and based on our observations that soleus was more susceptible to diet-induced IR than EDL, we performed total proteomics on soleus from the seven strains fed chow or WD to identify molecular signatures of muscle IR. We quantified 2885 proteins in at least 40 of 85 samples (**Dataset 1**). Hierarchical clustering revealed that the mean proteome clustered by strains but was largely refractory to diet effects (**Fig. 7A**), unlike metabolic traits, which clustered more strongly by diet (**Fig. 5**). This was also evident by pair-wise comparison of diet within each strain, which revealed very few proteins were significantly regulated by diet. For example, BALB had the most diet-regulated proteins of the strains (42 proteins) whereas A/J had the fewest (3 proteins) (**Fig. S4A**). Therefore, we assessed H2 of the proteome and the extent to which it is malleable by diet by partitioning the variances in expression of each protein into strain (H2), diet, or strain-by-diet (as in Fig. 3) (**Dataset 2**). Gene set analysis of the top 100 most heritable proteins (*i.e.* with the highest strain-derived variance; H2) revealed that pathways involved in translation, TCA cycle, respiratory electron transport, ATP synthesis, mitochondrial biogenesis and fatty acid beta-oxidation were among the most highly

overrepresented (**Fig. S4B**). Across the proteome, less variance was driven by diet compared to strain; however, for the proteins with the highest diet-derived variance, pathways involved in nuclear receptor signaling, cholesterol metabolism, and lipoprotein/chylomicron assembly and remodeling were among the most highly overrepresented (**Fig. S4B**).

To identify protein expression networks associated with Soleus GU:I, we built co-regulated protein networks using weighted gene co-expression network analysis (WGCNA) (Langfelder and Horvath, 2008). The resulting network consisted of seven modules (**Dataset 3**). The only modules that significantly correlated with Soleus GU:I were 'dark turquoise' and 'royal blue'. The 'dark turquoise' module was positively correlated with Soleus GU:I ($R = 0.785$, $p = 0.0009$; **Fig. 7B**) and negatively correlated with fasting plasma insulin ($R = -0.769$, $p = 0.0013$, **Fig. 7C**). Pathway analysis revealed that this module was highly overrepresented by glycolytic proteins (**Fig. 7D**). In fact, ten of eleven proteins in the canonical glycolytic pathway were present in the module, with the exception of HK2 (hexokinase 2). Also present in the module were two additional proteins linked to glycolysis, such as PGM1 (phosphoglucomutase 1), which catalyzes the bi-directional conversion of glucose-6-phosphate and the glycogen precursor glucose-1-phosphate, and the lactate transporter SLC16A3 (monocarboxylate transporter 4) (Bisetto et al., 2019) (**Fig. 7E**). Interestingly, expression of the ten glycolytic proteins present in the module varied by as much as four-fold across the groups (**Fig. 7F**), and each was among the top 11% of the most abundant proteins measured in the entire proteome (**Fig. S4C**), so we hypothesized that these variances in expression could alter metabolite flux at each of these steps along the glycolytic

pathway and have a major cumulative impact on total glycolytic flux. Diet was the greatest source of variance for these canonical glycolytic proteins (as opposed to strain or strain-by-diet interaction), and each was in the top 20% of diet-regulated proteins (**Fig. S4C**). The 'royal blue' module was also positively correlated with Soleus GU:I ($R = 0.67$, $p = 0.009$), and was not significantly correlated with fasting insulin. This module was overrepresented by mitochondrially localized proteins involved in carbonyl group metabolism associated with branched-chain amino acids (BCAAs), aldehydes and ketones (*i.e.* ACAD8, ECH1, ALDH2, ALDH6A1, HMGCL and OXCT1). Similar to the glycolytic proteins, diet was the greatest source of variance for these proteins, and each was in the top 5% of diet-regulated proteins (**Fig. S4C**). Changes in glycolytic and/or mitochondrial enzyme expression are often associated with muscle fiber type switching; however, chow-fed BALB, 129, BXD34, and ILSX97 had indistinguishable GU:I (**Fig. 2A, S2A**), whereas the soleus fiber type compositions were markedly different between these strains (**Fig. S5A-D**), with BALB and ILSX97 having the highest and lowest type 2a:1 ratio of all the strains, respectively. This indicates that fiber type composition can neither account for differences in soleus glucose uptake, nor for the difference in protein expression in the two correlating modules. Furthermore, there were no significant correlations between any of the muscle fiber type parameters and soleus glucose uptake (insulin stimulated or basal). Collectively, these data suggest that, although genetic effects were predominant in regulating the soleus proteome, diet-induced decreases in expression of proteins related to glycolysis, BCAA, aldehyde and ketone metabolism may underlie muscle IR.

T2D has been associated with decreased expression of the glucose transporter GLUT4 in adipose tissue and, in one study, specifically in oxidative muscle (Gaster et al., 2001; Stuart et al., 2013); however, GLUT4 (SLC2A4) expression in soleus did not significantly correlate with Soleus GU:I ($R = 0.34$, $p = 0.241$), nor did the other proteins along the canonical insulin signaling-GLUT4 pathway present in the dataset (IRS1, PDK1, PDK2, Akt2 and RAB10). These results were not surprising, as these proteins are primarily regulated via an insulin-responsive phosphorylation cascade rather than at the protein level. However, levels of RAB14, a Rab-GTPase implicated in muscle GLUT4 trafficking (Ishikura et al., 2007), positively correlated with GU:I ($R = 0.68$, $p = 0.007$), and so downregulation of this protein may be involved in muscle IR. In line with this, the most highly correlated protein with insulin-stimulated glucose uptake in our dataset was Profilin-2 (PFN2) ($R = 0.944$, $p = 3.95e-07$), also present in the glycolytic module. PFN2 is highly expressed in muscle and brain and, intriguingly, it is involved in endocytosis and plasma membrane trafficking (Gareus et al., 2006). Therefore, it is plausible that decreased PFN2 expression could lead to enhanced endocytosis, decreasing surface levels of GLUT4, diminishing insulin-stimulated glucose uptake.

These analyses of the soleus proteome have revealed that H2 is the primary driver of overall proteomic diversity, with proteins involved in translation and mitochondrial biology being the most heritable, but that diet especially impacts expression of proteins involved in cholesterol and lipoprotein metabolism. Furthermore, expression of a set of glycolytic proteins was most strongly correlated with soleus insulin responsiveness. This was driven by gene-by-diet interactions, such that WD had

strong effects on expression of these proteins in some strains, whereas the expression of these proteins was completely unaffected by WD in other strains.

DISCUSSION

Peripheral IR is frequently associated with obesity and hyperinsulinemia in humans and mouse models, but it has been difficult to disentangle the respective roles of these different parameters in metabolic disease. Such studies are challenging in humans because it is difficult to control the environment over the course of life. One of the most significant observations made in this study was the complete lack of correlation between insulin action in AT and muscle. This was most evident in A/J mice, where muscle was highly insulin responsive, whereas the AT were severely insulin resistant independent of diet, concomitant with enlarged adipocytes (**Fig 2A-C; 3A-D**). Our further investigation of A/J AT revealed intact insulin signaling, but very low levels of GLUT4 protein expression (**Fig. 3E-G**), which was the likely cause of the lack of insulin action in this tissue. Intriguingly, GLUT4 expression was not perturbed in muscle of A/J mice consistent with normal insulin action. These data are intriguing as previous studies have found that reducing GLUT4 levels selectively in AT by genetic manipulation results in whole-body insulin resistance (Abel et al., 2001). Based on these studies and the observation that GLUT4 levels in AT are reduced by approximately 50% in humans with T2D (Hammarstedt et al., 2012) and in WD-fed mice (Ikemoto et al., 1995), it has become widely accepted that adipocyte IR spreads via a systemic signal to other tissues including muscle. In contrast, our study suggests that, in some genetic

backgrounds, reduced adipocyte GLUT4 levels is insufficient to cause whole-body or muscle IR.

While adipocyte hypertrophy is widely regarded as metabolically unfavorable and linked with systemic IR (Jeong and Yoon, 2009), we observed that A/J mice fed WD had large, severely insulin resistant adipocytes, yet the muscle of this strain remained the most insulin responsive. This is exciting, as previous studies comparing metabolic responses between A/J and BL/6 reported that, while BL/6 exhibited classical phenotypes associated with the metabolic syndrome in response to WD, A/J became obese but metabolically protected after WD feeding (Surwit et al., 1988). Conversely, BXD34 displayed only a minimal increase in adiposity and adipocyte size in response to WD, yet the BXD34 soleus developed IR in response to WD. These data suggest that the expansion of AT during a positive energy balance is key to sustained metabolic health. Specifically, we hypothesize that the efficient ability of the A/J adipocytes to expand in size to facilitate lipid storage protects these mice from systemic IR, and that an inability of the BXD34 adipocytes to enlarge for efficient lipid storage has a negative consequence on glucose metabolism by muscle. This is consistent with previous studies showing that specific manipulations that increase circulating lipids are sufficient to cause muscle IR (Boden et al., 2001; Roden et al., 1996). Consistent with the efficient lipid storage model providing protection against metabolic dysfunction, A/J mice were protected from diet-induced liver triglyceride accumulation and serum dyslipidemia compared to BL/6 (Sinasc et al., 2016). These data suggest that enlarged adipocytes are prone to IR, likely through decreased GLUT4 protein levels, but that insulin resistant adipocytes do not cause muscle IR. On the contrary, we suggest that the ability of the

AT to store excess dietary fat, whether by hypertrophy or hyperplasia, benefits systemic and muscle glucose metabolism by protecting these tissues from lipotoxicity. Further studies in diverse strains such as A/J and BXD34 should hone in on the mechanisms that govern intrinsic differences between individuals in adipocyte size and expandability, and the systemic effects on metabolism.

Intriguingly, there was only a weak correlation in insulin responsiveness between soleus and EDL. This likely reflects the different properties of these muscles: soleus is a highly oxidative tonic muscle, whereas EDL is comparatively 'fast-twitch' with a higher proportion of glycolytic fibers. Tonic muscles are highly reliant on exogenous substrates, such as fatty acids and glucose, to meet a constant energy demand. Thus, we propose the elevated insulin responsiveness of the soleus is related to an insulin-induced switch to glucose utilization after a meal, rendering the soleus more susceptible to diet-induced IR compared to phasic muscles such as EDL, which are rich in glycogen stores and less reliant on uptake of exogenous glucose (TeSlaa et al., 2021). Taken together, these results indicate that studies in only one muscle, or even a biopsy limited to a certain region of a muscle, would not accurately reflect responses across all muscle groups.

Our analysis of the soleus proteome revealed a strong positive correlation between soleus insulin responsiveness and the expression of ten canonical glycolytic enzymes (**Fig. 7B-F**). This is an exciting observation because it emphasizes the potentially important role of glycolytic flux as a determinant of muscle insulin action. Conversely, previous studies have claimed that the principal fate of glucose taken up by muscle is either incorporation into glycogen or mitochondrial oxidation. Consistent with the important role of glycolysis in muscle, recent studies examining the distribution of

¹³C-glucose in young C57Bl/6N male mice have revealed that circulating glucose strongly labels glycolytic intermediates in specific mouse tissues, particularly soleus, and the majority of this glycolytic flux is channeled toward lactate production (TeSlaa et al., 2021) rather than being oxidized in mitochondria. Furthermore, we have previously shown that increasing mitochondrial glucose oxidation was not sufficient to increase muscle GU:I (Small et al., 2018). Hence, this raises the possibility that glycolysis represents a major driver of insulin responsiveness in muscle and that muscle IR is accompanied by a shift in energy utilization from exogenous carbohydrates, fatty acids and ketones toward protein catabolism. In line with this, muscle wasting (sarcopenia) is a common complication of IR (Guerrero et al., 2016; Guillet and Boirie, 2005). Notably, the conventional view is that in T2D there is a shift in the muscle machinery away from mitochondrial fatty acid oxidation (Mootha et al., 2003; Simoneau and Kelley, 1997) and it was assumed this is accompanied by a shift toward glycolysis. Based on our data, we predict this is unlikely. Our analysis also revealed a positive correlation between soleus insulin responsiveness and expression of mitochondrial enzymes involved in carbonyl group metabolism such as BCAAs, aldehydes and ketones. This is intriguing, as BCAAs have been shown to induce muscle IR in the context of a high fat diet by causing accumulation of short-chain acyl-carnitine metabolites (Newgard et al., 2009; White et al., 2016); therefore, our data suggest accumulation of such metabolic intermediates may be a consequence of decreased expression of these enzymes in muscle IR. Because this significant decline in proteins involved in carbonyl group metabolism in insulin resistant muscle was not associated with a parallel increase in glycolytic capacity, but rather the opposite, we propose that this reflects the true fate of glucose in muscle.

It is notable that the differences we observed in glycolytic protein levels were as great as four-fold and that ten of eleven canonical glycolytic proteins were coordinately regulated in our dataset (**Fig. 7E-F**). Previous studies have suggested that glycolytic flux is governed by four major rate-limiting steps, which include glucose transport, hexokinase, PFK and LDH (Tanner et al., 2018). In these studies, only the consequences of raising the levels of each glycolytic enzyme alone on pathway flux was examined, so it is conceivable that coordinate regulation of the entire glycolytic pathway, as we observed in insulin sensitive muscle, could cause a substantial change in glucose utilization (Vander Heiden et al., 2009). Such glycolytic regulation appears to have broader disease relevance, as several transcriptomic datasets from human muscle have identified glycolytic enzymes including LDHB and HK2 as among the genes most downregulated in IR and/or T2D (Fueger et al., 2007; Palsgaard et al., 2009; Sears et al., 2009). Consistent with this, it has been observed that overexpression of the enzyme PFKFB3, a major activator of glycolysis, in muscle caused increased glucose disposal, leanness and increased metabolic rate under chow and WD fed conditions (Xiang et al., 2021). Similarly, deletion of AMPK in mouse muscle was found to paradoxically enhance insulin sensitivity at least in part by causing a compensatory increase in glycolysis (Lantier et al., 2020). Thus, optimal insulin sensitivity may be set both by the efficiency with which muscle can metabolize glucose via glycolysis to lactate, and fatty acids to CO₂ in mitochondria, thus providing a degree of mutual exclusivity in the fate of these different nutrients. Increased glycolysis could also protect against increased mitochondrial reactive oxygen species production, a potential mechanism of muscle IR. We propose that this balance may provide a major regulator of muscle insulin responsiveness. Our data indicate the changes in glycolytic and mitochondrial proteins

we observed were not due to changes in muscle fiber types (**Fig. S5**), so the underlying cause for changes in the expression of these enzymes should be further investigated.

STUDY LIMITATIONS

We acknowledge several limitations of our study. First, we only measured the effects of insulin on glucose uptake, as this is the aspect of insulin action most directly related to normoglycemia, and IR is classically defined as a deficiency in glucose uptake at a given insulin dose. However, it would be of interest to interrogate strain-by-diet interactions on other insulin mediated processes such as protein synthesis and lipid metabolism, as IR has been reported to be selective primarily for glucose metabolism (Tan et al., 2015). Second, we primarily investigated insulin action at only one dose of insulin, precluding us from obtaining insulin sensitivity data at submaximal insulin doses, however, GU:I into muscle is defective at all doses in humans with IR or T2D (James et al., 2021; Kolterman et al., 1980). Third, our study is limited to adolescent male mice. It is well established that sex differences affect susceptibility to obesity and IR in both mice and humans, such that females tend to have improved metabolic profiles (Karp et al., 2017; Mittelstrass et al., 2011; Norheim et al., 2019; Parks et al., 2015). Finally, we have only examined the characteristics of epididymal fat pads and so these studies should be expanded to include additional fat depots.

CONCLUSIONS

Here we utilized genetic and environmental diversity to elucidate GxE interactions on tissue-specific and whole-body measures of insulin action. This has deconvoluted extensive GxE interactions on IR-associated traits and revealed a profound disconnect between IR in skeletal muscle and AT. Moreover, we demonstrated that differences in adipocyte size or GLUT4 expression did not dictate skeletal muscle insulin responsiveness. Rather, we demonstrate that hyperinsulinemia was invariably present in mice with muscle IR, and proteomics analysis of soleus muscle revealed decreased glycolytic capacity as a potential mechanistic link. These studies provide researchers with information regarding model selection for dietary studies, and future studies should expand on the genetic backgrounds and environmental interventions studied here to increase the applicability to diverse populations.

ACKNOWLEDGEMENTS

We thank Prof. Jake Lusis (University of California Los Angeles) for insightful discussions about mouse strain diversity and metabolic phenotyping. We thank technical staff at Australian BioResources (Mossvale, NSW, AU) and in the Laboratory Animal Services at the Charles Perkins Centre of the University of Sydney. We thank Dr. Courtney Wright of Sydney Microscopy and Microanalysis for performing the digital scanning of histology slides. We thank Assoc. Prof. Kim Bell-Anderson (University of Sydney) for her helpful guidance using the Promethion equipment. EchoMRI was performed in the Sydney Imaging Facility, University of Sydney. Proteomics was performed in the Sydney Mass Spectrometry Facility, Charles Perkins Centre,

University of Sydney. Histology was performed in the Histopathology Facility of the Garvan Institute of Medical Research. This work was supported by National Health and Medical Research Council (NHMRC) Project Grant GNT1086851 (to D.E.J.). D.E.J. is an ARC Laureate Fellow. The content is solely the responsibility of the authors and does not necessarily represent the official views of the NHMRC or ARC. A.M.F. was supported by a postdoctoral research grant from the Benzon Foundation. Furthermore, A.M.F. was funded by Danish Diabetes Academy, funded by the Novo Nordisk Foundation, grant number NNF17SA0031406. I.H.T. was funded by a scholarship from the Novo Nordisk Foundation, grant number NNF16OC0023080.

AUTHOR CONTRIBUTIONS:

D.E.J., G.J.C., M.E.N., A.M.F., I.H.T., S.M., J.S. and K.C.C. designed the study. M.E.N., S.M., K.C.C., A.M.F., I.H.T., J.S., S.W.C.M., F.C.W., M.P., S.L.H., D.J.F., A.E.B., S.T. and G.J.C. performed experiments. J.S. and K.C.C. developed the methods for *ex vivo* glucose uptake into muscle and AT, respectively. M.E.N. performed quantification of adipocyte size. S.W.C.M. performed Western blotting and qPCR in AT. S.L.C. performed the mass spectrometry proteomics. K.C.C. and S.W.C.M. performed muscle fiber typing sample processing and quantification. M.M.S provided statistical advice for heritability analyses and WGCNA analyses. A.M.S. provided statistical advice for MCMCglmm modeling. M.E.N. and S.M. generated the figures and performed the statistical analyses. M.E.N., S.M., J.S., S.W.C.M. and D.E.J. wrote the manuscript with input from all the authors.

Declaration of Interests: The authors declare no competing interests.

MAIN FIGURE TITLES AND LEGENDS

FIGURE 1. Metabolic traits across thirteen mouse strains and two diets. (A)

Adiposity, six-hour fasting (B) blood glucose and (C) serum insulin concentrations, and (D) blood glucose concentration area under the curve (AUC) during oral glucose tolerance test in thirteen mouse strains fed chow or WD. Bars represent group means and points represent individual mice. Error bars represent means \pm SEM. Significant differences by a two-way ANOVA, followed by a Tukey's post hoc test. * indicate a significant difference between chow and WD within a strain, # indicate a significant difference between BL/6 and another strain within the same diet; $p < 0.05$. See also Figure S1.

FIGURE 2. Muscle and adipose tissue insulin responsiveness. Insulin-stimulated (10nM) *ex vivo* glucose uptake into intact (A) soleus and (B) EDL or (C) minced epididymal white adipose tissue from seven mouse strains fed chow or WD. Error bars represent means \pm SEM. These data are repeated in Fig. S2 for comparison of insulin-stimulated versus basal values. Fold insulin-stimulated over basal glucose uptake for (D) soleus, (E) EDL or (F) adipose tissue. Significant differences by a two-way ANOVA, followed by a Tukey's post hoc test. * indicate a significant difference between chow and WD within a strain; $p < 0.05$. See also Figure S2.

FIGURE 3. Adipose tissue characterization. (A) Representative H&E stained sections of fixed epididymal white adipose tissue (EpiWAT) from each strain and diet group (Scale bar represents 100 μ m). (B) Tail probability density plots with interquartile range (IQR) of epididymal adipocyte areas pooled by group and (C) median adipocyte area of each mouse represented by points and the group averages represented by bars. (D) Insulin-stimulated *ex vivo* glucose uptake into EpiWAT from chow-fed BL/6 or A/J mice and with varying doses of insulin. Error bars represent means \pm SEM (n=3). EpiWAT of chow-fed BL/6 or A/J mice, Western blotting for protein expression of (E) total and phosphorylated Akt in response to +/- 10 nM insulin and (F) GLUT4, and (G) *Glut4* mRNA expression by qPCR, expressed as fold of BL/6. For F-G, Error represents means \pm SEM. Significant differences by Student's t-test. * indicates a significant difference of $p < 0.05$; ** indicates a significant difference of $p < 0.01$.

FIGURE 4. Variance partitioning of metabolic traits. Variances across the seven selected mouse strains and two diets for metabolic traits were partitioned using linear mixed-effect models into strain (broad-sense heritability; H²), diet, strain-by-diet and residual.

FIGURE 5. Metabolic trait clustering by strain and diet. Heatmap of Z-scored group data with hierarchical clustering of selected metabolic traits related to tissue glucose

uptake and indices of insulin resistance across the seven strains fed chow or WD. See also Figure S3.

FIGURE 6. Metabolic trait correlation networks. (A) Correlation coefficient matrix of the metabolic traits from the seven mouse strains followed by hierarchical clustering. * indicates a significant correlation. (B) Network of significant correlations with tissue insulin-stimulated glucose uptake was generated to illustrate metabolic network connectivity.

FIGURE 7. Analysis of the soleus proteome. Total proteomics of soleus from the seven mouse strains fed two diets. (A) Hierarchical clustering of the mean proteome. Protein module in soleus correlates with (B) soleus glucose uptake and (C) fasting serum insulin, and (D) pathway analysis of module. (E) Schematic of canonical glycolysis pathway (green box), with proteins within the glycolytic module in black, and proteins absent from the module in white. PGM1 (involved in glycogen storage and breakdown; purple box) and SLC16A3 (a lactate transporter; orange box) also within glycolytic module. Boxplots of Log₂ LFQ intensity values of (F) the glycolytic proteins depicted in (E). See also Figures S4 and S5, Supplemental Table 1, and Supplemental Datasets 1-3.

STAR METHODS

Resource Availability

Lead Contact

Further information and requests for resources and reagents should be directed to and will be fulfilled by the lead contact, David E. James (david.james@sydney.edu.au).

Materials Availability

- The GLUT4 antibody was generated by the David James laboratory (James et al., 1989) and is available upon request.

Data and Code Availability

- Proteomics data have been deposited at PXD029680 and are publicly available as of the date of publication. DOI is listed in the key resources table.
- This paper does not report original code.
- Any additional information required to reanalyze the data reported in this paper is available from the lead contact upon request.

Animals

C57BL/6J (BL/6), BXH9/TyJ (BXH9), BALB/cJ (BALB), BXD34/TyJ (BXD34), ILSXISS97 (ILSX97), AKR/J (AKR), DBA/2J (DBA), ILSXISS50 (ILSX50), ILSXISS89 (ILSX89), ILSXISS98 (ILSX98) and NOD/ShiLtJ (NOD) inbred mouse strains were obtained from Australian BioResources (Moss Vale, NSW, Australia). A/J and 129X1/SvJ (129) inbred mouse strains were obtained from Animal Resources Centre (Perth, WA, Australia). Experiments were performed in accordance with NHMRC (Australia) guidelines and under the approval of The University of Sydney Animal Ethics Committee. Mice were monitored at least twice per week and weighed weekly.

Male littermates were randomly assigned to cages upon weaning at 6 weeks of age, 3 to 5 per cage, maintained at 23°C on a 12 hour light/dark cycle and given *ad libitum* access to water and standard laboratory chow containing 12% calories from fat, 65% calories from carbohydrate, 23% calories from protein ('Irradiated Rat and Mouse Diet', Specialty Feeds, Glen Forest, WA, Australia). Mice were acclimatized in the Laboratory Animal Services Facility (Charles Perkins Centre, University of Sydney) for 1 week prior to experimentation. From 8 to 10 weeks of age, mice were given *ad libitum* for a total of 8 weeks either the standard laboratory chow or a high fat, high sucrose Western diet (WD) made in-house containing 45% calories from fat, 36% calories from carbohydrate and 19% calories from protein. Specifically, the WD contained: 3.5%g cellulose, 4.5%g bran, 13%g cornstarch, 21%g sucrose, 16.5%g casein, 3.4%g gelatine, 2.6%g safflower oil, 18.6%g lard, 1.2%g AIN-93 vitamin mix (MP Biomedicals), 4.95%g AIN-93 mineral mix (MP Biomedicals), 0.36%g choline and 0.3%g L-cysteine.

Blood collections

Mice were fasted for 6 hours before being restrained to allow puncture and blood collection from the saphenous vein. Blood was collected into EDTA coated tubes on ice and centrifuged at 2,000 x g for 15 minutes to separate plasma.

Whole-Body Metabolic Measures

Mice were placed in metabolic cages, Promethion (Sable Systems International), at 5-6 weeks of diet intervention to assess activity and food intake. Fat and lean mass measures were acquired via EchoMRI-900 (EchoMRI Corporation Pte Ltd, Singapore) after 7 weeks of diet.

Fasting insulin levels were measured in plasma from 6-hour fasted mice an Insulin Mouse Ultra Sensitive ELISA (Crystal Chem USA, Elk Grove Village, Illinois, USA) according to the manufacturer's protocol. An oral glucose tolerance test (GTT) was performed on mice after 7 weeks of diet. 6-hour fasted mice were dosed via oral gavage of 25% glucose in water at 2 mg/kg lean mass. Blood glucose concentration was measured directly from tail whole blood via a glucose monitor (Accu-Chek, Roche Diabetes Care, NSW, Australia) at 0, 15, 30, 45, 60, 90 and 120 minutes after administration of glucose. Blood insulin levels during the oGTT were measured by collecting 5 μ L of tail whole blood at 0, 5, 10 and 30 minutes directly into an insulin ELISA plate containing sample diluent. The assay was then performed according to the

manufacturer's protocol. The resulting whole blood concentrations were multiplied by a factor of 2 to estimate plasma concentrations.

An intraperitoneal insulin tolerance test (ipITT) was performed on mice after 6 weeks of diet. 2-hour fasted mice were dosed via intraperitoneal injection of insulin in PBS at 1 U/kg lean mass. Blood glucose was sampled from the tail vein at 0, 5, 10, 20 and 30 minutes after administration of insulin.

***Ex vivo* glucose uptake**

For *ex vivo* glucose uptake, mice were euthanized by cervical dislocation followed by dissection of epididymal adipose tissue, soleus and extensor digitorum longus (EDL) tissues. Glucose uptake into both the soleus and EDL was assessed by mounting the tissue and incubating the tissue for 30 minutes in Krebs Henseleit buffer containing 5.5 mM glucose, 2 mM pyruvate and 0.1% BSA (KRH) that had been gassed with carbogen (95% O₂/5% CO₂). 0.375 μ Ci/ml [³H]-2-deoxyglucose (2-DG) and 0.05 μ Ci/ml [¹⁴C]-Mannitol was incubated with the muscle samples with or without 100 nM insulin for 20 minutes at 30°C followed by washing in ice-cold PBS and then snap frozen. Samples were lysed in 250 mM NaOH at 70°C. Epididymal adipose tissue was finely chopped and incubated for 2 to 4 hours in 25 mM glucose containing DMEM with pyruvate containing 25 mM HEPES and 2% BSA. Explants were then incubated in KRP containing 25 mM HEPES and 2% BSA, stimulated for 20 minutes with 0 nM or 10 nM insulin followed by addition of 50 μ M 2-DG, 1 μ Ci [³H]-2-DG and 0.14 Ci [¹⁴C]-mannitol

for the final 5 minutes. Samples were washed 3x in ice-cold PBS and then lysed in 100 mM NaOH.

Tracer in the muscle and adipose tissue lysates was quantified by liquid scintillation counting and [³H]-2-DG was corrected for extracellular [¹⁴C]-mannitol then normalised to wet weight of the tissue for soleus and EDL or protein concentration as measured by a BCA assay for the adipose tissue. Because of the significant expansion of the fat content of adipose tissue with WD, we normalized adipose glucose uptake to mg protein rather than tissue wet weight as is common practice for muscle.

Underscoring the effectiveness of this normalization method for the adipose tissue, WD had no effect on basal GU, with the exception of a significant increase in BXH9 compared to chow (**Fig. S2C**).

Statistical outliers (>2 standard deviations from the group means) were removed from the muscle glucose uptake datasets (<15% of data points). Fold glucose uptake was calculated as insulin over the mean basal value of each group for soleus and EDL, and as insulin over basal for each individual animal for adipose tissue.

Proteomics sample preparation

Soleus muscle was snap frozen with liquid nitrogen and pulverised before resuspension in 200 μ L of 4% sodium deoxycholate in 100 mM Tris pH 8 buffer and heated at 95°C for 10 minutes. Samples were homogenised by bead beating in a TissueLyzer with a stainless bead for 1 minute at 30 Hz. Lysates were centrifuged at 13,000 x g for 10 min to pellet insoluble cell debris and protein concentration in

supernatant was determined by BCA assay. 10 µg of protein was aliquoted into a 250 µL deep well plate and volume adjusted to 20 µL with water before 1 µL of reduction/alkylation (10 mM TCEP, 40 mM CAA) buffer was added and the plate incubated for 20 minutes at 60°C. Once cooled to room temperature, 0.4 µg trypsin and 0.4 µg LysC was added to each sample and incubated overnight (18 h) at 37°C with gentle agitation. 30 µL water and 50 µL 1% TFA in ethyl acetate was added to stop digestion and dissolve any precipitated SDC. Samples were prepared for mass spectrometry analysis by StageTip clean up using SDB-RPS solid phase extraction material (Rappsilber et al., 2007). Briefly, 2 layers of SDB-RPS material was packed into 200 µL tips and washed by centrifugation of StageTips at 1,000 x g for 2 minutes in a 96-well adaptor with 50 µL acetonitrile followed by 0.2% TFA in 30% methanol and then 0.2% TFA in water. 50 µL of samples were loaded to StageTips by centrifugation at 1,000 g for 3 minutes. Stage tips were washed with subsequent spins at 1,000 g for 3 minutes with 50 µL 1% TFA in ethyl acetate, then 1% TFA in isopropanol, and 0.2% TFA in 5% ACN. Samples were eluted by addition of 60 µL 60% ACN with 5% NH₄OH₄. Samples were dried by vacuum centrifugation and reconstituted in 30 µL 0.1% TFA in 2% ACN.

Proteomics data processing and analysis

Samples were analysed using a Dionex UltiMate™ 3000 RSLCnano LC coupled to a Exploris Orbitrap mass spectrometer. 3 µL of peptide sample was injected onto an in-house packed 75 µm × 40 cm column (1.9 µm particle size, ReproSil Pur C18-AQ) and separated using a gradient elution, with Buffer A consisting of 0.1% formic acid in

water and Buffer B consisting of 0.1% formic acid in 80% ACN. Samples were loaded to the column at a flow rate $0.5 \mu\text{L min}^{-1}$ at 3% B for 14 minutes, before dropping to $0.3 \mu\text{L min}^{-1}$ over 1 minute and subsequent ramping to 30% B over 110 min, then to 60% B over 5 minutes and 98% B over 3 minutes and held for 6 minutes, before dropping to 50% and increasing flow rate to $0.5 \mu\text{L min}^{-1}$ over 1 minute. Eluting peptides were ionized by electrospray with a spray voltage of 2.3 kV and a transfer capillary temperature of 300°C . Mass spectra were collected using a DIA method with varying isolation width windows (widths of m/z 22-589) between 350 - 1650 according to **Supplemental Table 1**. MS1 spectra were collected between m/z 350 - 1650 m/z at a resolution of 60,000. Ions were fragmented with an HCD collision energy at 30% and MS2 spectra collected between m/z 300-2000 at resolution of 30,000, with an AGC target of $3e5$ and the maximum injection time set to automatic. Raw data files were searched using DIA-NN using a library free FASTA search against the reviewed UniProt mouse proteome (downloaded May 2020) with deep learning enabled (Demichev et al., 2019; Rappsilber et al., 2007). The protease was set to Trypsin/P with 1 missed cleavage, N-term M excision, carbamidomethylation and M oxidation options on. Peptide length was set to 7-30, precursor range 350-1650, and fragment range 300-2000, and FDR set to 1%. Missingness per sample was $<10\%$. Proteins that were found in <40 samples were filtered away and remaining missing values were imputed by substitution with a value randomly generated from within the standard deviation around the mean for the protein (Supplemental Dataset 1). The mass spectrometry proteomics data have been deposited to the ProteomeXchange Consortium via the PRIDE partner repository (Perez-Riverol et al., 2019) with the dataset identifier PXD029680.

Equations for insulin sensitivity indices

HOMA-IR:

$$\frac{\text{fasting glucose } \left(\frac{\text{mM}}{\text{L}}\right) * \text{fasting insulin } \left(\frac{\mu\text{U}}{\text{mL}}\right)}{22.5}$$

QUICKI:

$$\frac{1}{\log \left[\text{fasting insulin } \left(\frac{\mu\text{U}}{\text{mL}}\right) \right] + \log \left[\text{fasting glucose } \left(\frac{\text{mg}}{\text{dL}}\right) \right]}$$

GI ratio:

$$\frac{\text{fasting glucose } \left(\frac{\text{mM}}{\text{L}}\right)}{\text{fasting insulin } \left(\frac{\text{ng}}{\text{mL}}\right)}$$

Matsuda index:

$$\frac{10,000}{\sqrt{\left[\text{fasting glucose } \left(\frac{\text{mg}}{\text{dL}}\right) * \text{fasting insulin } \left(\frac{\mu\text{U}}{\text{mL}}\right) \right] * \left[\text{mean glucose during GTT } \left(\frac{\text{mg}}{\text{dL}}\right) * \text{mean insulin during GTT } \left(\frac{\mu\text{U}}{\text{mL}}\right) \right]}}$$

IRI:

$$\text{GTT AUC} * \text{fasting insulin } \left(\frac{\text{ng}}{\text{mL}}\right)$$

Adipocyte area

Formalin-fixed epididymal adipose tissue was paraffin embedded, sectioned, mounted on coverslips and stained with H&E. Coverslips were scanned to digital images using an Aperio ScanScope. Adipocyte cell area was then analyzed in ImageJ version 1.51. Briefly, images were converted to 8 bit and the threshold was adjusted so

cell membranes were identified as signal and cell contents were identified as background. The “Find Edges” built-in function was applied, and the color was inverted. The “Analyze Particles” built-in function was then applied to calculate cell areas with a defined size range of 400-80000 μm^2 and a circularity range of 0.40-1.00. For each mouse, two random areas within a slide were analyzed so that >1000 adipocytes were quantified per mouse. Tail probability plots were generated using the R package ggplot2 version 3.3.2.

Western blotting

Epididymal adipose tissue from chow-fed BL/6 and A/J mice was excised and finely chopped with scissors in DMEM containing 25 mM glucose, 5 mM pyruvate, 25 mM HEPES and 2% BSA. Each explant was divided into two aliquots and either stimulated for 20 minutes with 10 nM insulin or served as an unstimulated control so that basal and insulin stimulated samples were collected for each animal. Explants were then washed 3x with PBS and frozen at -80°C before being lysed in RIPA buffer (50 mM Tris-HCl pH 8.0, 250 mM NaCl, 5 mM EDTA, 1% Triton X-100) containing protease inhibitors (1 mM sodium pyrophosphate, 2 mM sodium orthovanadate, 10 mM sodium fluoride) by sonication. Protein concentrations were determined by BCA assay and adjusted to 2 mg/mL.

10 μg of protein was resolved by SDS-PAGE, transferred onto PVDF membranes and blocked in TBS-T (0.1 % Tween in Tris-buffered saline) containing 2% skim milk for 1 hour. Membranes were then washed 3 x 10 minutes in TBS-T and incubated

overnight in primary antibodies against phosphorylated Akt T308 (Cell Signaling Technologies #2965; diluted 1:1000), pan-Akt (Cell Signaling Technologies #9272; diluted 1:1000), GLUT4 (developed in-house (James et al., 1989); diluted 1:1000), and 14-3-3 (Santa Cruz #sc-1657; diluted 1:5000). The following day membranes were washed 3 x 10 minutes in TBS-T and incubated for 1 hour in species-appropriate fluorescent secondary antibodies. Imaging and densitometry were performed using LICOR Image Studio.

qPCR

RNA was extracted from frozen chow-fed BL/6 and A/J epididymal adipose tissue using TRIzol reagent and phase separation with 1-bromo-3-chloropropane. cDNA synthesis was carried out by PrimeScript cDNA synthesis kit according to manufacturer's instructions. qPCR was performed on a QuantStudio 6 PCR System using FastStart Universal SYBR Green Master (Roche Applied Science) with the primer sets against *mGlut4* (F: gccacgatggagacatagc, R: gacggacactccatctgttg) and *mCypB* (F: acctccgtaccacatccat, R: ttcttcataaccacagtcaagacc). Relative gene expression was determined using the $\Delta\Delta\text{Ct}$ method.

Muscle fiber typing

Immunofluorescent fiber staining of mouse soleus muscles was adapted from (Bloemberg and Quadrilatero, 2012). Soleus muscles of mice were excised and frozen

in OCT in an isopentane slurry over liquid nitrogen and stored at -80°C . The muscles were sectioned on a cryostat at $10\ \mu\text{M}$ thickness and mounted onto slides. Sections were blocked in 10% horse serum in PBS for 1 hour. Primary antibody mixtures containing MHCI (BA-F8, 1:50), MHCIIa (SC-71, 1:600) and MHCIIb (BF-F3, 1:100) from the Developmental Studies Hybridoma Bank (University of Iowa) were diluted in 10% horse serum and applied to the sections for 2 hours. Sections were washed 3 x 5 minutes in PBS before being incubated for 1 hour with a second antibody cocktail containing Alexa Fluor 488 IgG2b (Life Technologies, green, 1:500), Alexa Fluor 555 IgG1 (Life Technologies, red, 1:500), Alexa Fluor 350 IgM (Life Technologies, blue, 1:500) and Lectin from *Triticus vulgaris*-Atto 488 conjugate (Sigma, green, 1:500). Sections were washed 3 x 5 minutes in PBS and mounted using Immuno-Fluore mounting medium (MP Biomedical). Slides were imaged using the Zeiss Axio Vert A1 microscope across the entire cross-section and assembled into a composite image using ImageJ. Fibers were manually counted using the lectin stain to denote cell boundaries and assigned as being green (type 1), red (type 2a), blue (type 2b) or unstained (type 2x).

Variance estimates and means comparisons

Overall strain, diet or strain-by-diet effects were tested on log-transformed data to achieve normal Gaussian distribution (with the exception of QUICKI, which is already on a log scale as calculated) by two-way ANOVA with an alpha of $p < 0.05$, and differences between group means were subsequently tested by Tukey's post-hoc, using base R functions, unless otherwise specified in the figure legends. Pairwise comparison of

proteins within each strain was conducted using the R Limma package (Ritchie et al., 2015). Group data plots were generated using the R package ggplot2 version 3.3.2.

Variance partitioning analyses (heritability)

Data were first log-transformed to achieve normal Gaussian distributions. Variances were partitioned using a linear random slopes model with diet and strain as random effects. To estimate variance derived from strain-by-diet interactions, a synthetic cohort was created for each trait by subtracting WD from chow log-normalized values for each possible WD:chow animal combination, then 4 values for each WD animal were randomly sampled using the function `sample_n` from the R package `dplyr` version 1.0.2. For this linear model, strain was defined as a random factor. The total variance from this model was calculated by summing strain and residual variances. The proportion of the total variance explained by strain was scaled to explain a portion of the residual variance from the previous model as strain-by-diet interaction. Linear modeling was performed using lme functions from the R package `lme4` version 1.1-25. Variance plots were generated using the R package `ggplot2` version 3.3.2.

Trait-by-trait correlations

Trait by trait correlations including multi-level data augmentation for missing trait data were performed under Bayesian mixed models framework using the R package `MCMCglmm` version 2.29 (Hadfield and Others, 2010). Data were first log-transformed to achieve normal Gaussian distributions (with the exception of QUICKI, which is

already on a log scale as calculated). To achieve a multi-response model, traits were defined as response variables. Gaussian distributions were specified for each response variable. An inverse Wishart prior belief parameter was defined as $\nu=0.002$. The model was then run for 2 million iterations with a burn-in phase of 40,000 and a thinning interval of 40. Mean posterior distributions of the variance-covariance matrix were then converted to correlation coefficients. The analysis was repeated 3 times and the mean correlation coefficients were used to generate a correlation matrix. The correlation matrix heatmap with Euclidean distance clustering was generated using the R package `heatmap.2`. A correlation was considered significant if the 95% credible intervals did not span 0. For the metabolic trait correlation network plot was generated using the R package `ggraph` version 2.0.3.

Protein network construction

Proteins that did not map to unique protein groups were filtered away and individual proteins were averaged across strain and diet. Clustering was performed on scaled data using the average linkage method in the R base function `hclust`. A weighted protein co-expression network was constructed using the R package `WGCNA` (Langfelder and Horvath, 2008). The network was built using a soft power of 10, minimum module size 15 and a tree cut height of 0.2. Biological pathway overrepresentation analysis was performed for KEGG pathways in the R package `WebGestaltR` (Zhang et al., 2005), with the minimum number of genes in a pathway specified as 15 and maximal as 200. Pathways with <0.05 false discovery rate (FDR) were considered to be significantly overrepresented.

STAR METHODS KEY RESOURCES TABLE

REAGENT or RESOURCE	SOURCE	IDENTIFIER
Antibodies		
Akt T308	Cell Signaling	Cat# 2965
Total Akt	Cell Signaling	Cat# 9272
GLUT4	James et al., 1989	
14-3-3	Santa Cruz	Cat# 1657
Myosin heavy chain Type I	Developmental Studies Hybridoma Bank (University of Iowa)	Cat# BA-F8
Myosin heavy chain Type IIa	Developmental Studies Hybridoma Bank (University of Iowa)	Cat# SC-71
Myosin heavy chain Type IIb	Developmental Studies Hybridoma Bank (University of Iowa)	Cat# BF-F3

Alexa Fluor 488 IgG2b	Life Technologies Australia	Cat# A- 11094
Alexa Fluor 555 IgG1	Life Technologies Australia	Cat# A- 21127
Alexa Fluor 350 IgM	Life Technologies Australia	Cat# A- 31552
Lectin from Triticus vulgaris-Atto 488 conjugate	Sigma-Aldrich	Cat#16441
Bacterial and virus strains		
Biological samples		
Chemicals, peptides, and recombinant proteins		
Critical commercial assays		
Insulin Mouse Ultra Sensitive ELISA	Crystal Chem USA (Elk Grove Village, IL, USA)	Cat# 90080
Deposited data		
Proteomics dataset	ProteomeXchange Consortium	PXD029680
Experimental models: Cell lines		
Experimental models: Organisms/strains		
C57BL/6J	Australian BioResouces (Moss Vale, NSW, AU)	

BXH9/TyJ	Australian BioResouces (Moss Vale, NSW, AU)	
BALB/cJ	Australian BioResouces (Moss Vale, NSW, AU)	
ILSXISS97	Australian BioResouces (Moss Vale, NSW, AU)	
ILSXISS50	Australian BioResouces (Moss Vale, NSW, AU)	
ILSXISS89	Australian BioResouces (Moss Vale, NSW, AU)	
ILSXISS98	Australian BioResouces (Moss Vale, NSW, AU)	
AKR/J	Australian BioResouces (Moss Vale, NSW, AU)	
DBA/2J	Australian BioResouces (Moss Vale, NSW, AU)	
NOD/ShiLtJ	Australian BioResouces (Moss Vale, NSW, AU)	
A/J	Animal Resources Centre (Perth, WA, AU)	
129X1/SvJ	Animal Resources Centre (Perth, WA, AU)	

Oligonucleotides		
Recombinant DNA		
Software and algorithms		
MCMCgIimm version 2.29	Hadfield et al., 2010	
WGCNA	Langfelder and Horvath, 2008	
WebGestaltR	Zhang et al., 2005	
Other		
Chow diet	Gordon's Specialty Stock Feeds (Yanderra, NSW, AU)	
AIN-93 vitamin mix	MP Biomedicals (Seven Hills, NSW, AU)	
AIN-93 mineral mix	MP Biomedicals (Seven Hills, NSW, AU)	

REFERENCES

Abel, E.D., Peroni, O., Kim, J.K., Kim, Y.B., Boss, O., Hadro, E., Minnemann, T., Shulman, G.I., and Kahn, B.B. (2001). Adipose-selective targeting of the GLUT4 gene impairs insulin action in muscle and liver. *Nature* 409, 729–733.

Bisetto, S., Wright, M.C., Nowak, R.A., Lepore, A.C., Khurana, T.S., Loro, E., and Philp, N.J. (2019). New Insights into the Lactate Shuttle: Role of MCT4 in the Modulation of

the Exercise Capacity. *iScience* 22, 507–518.

Bloemberg, D., and Quadrilatero, J. (2012). Rapid determination of myosin heavy chain expression in rat, mouse, and human skeletal muscle using multicolor immunofluorescence analysis. *PLoS One* 7, e35273.

Boden, G., Lebed, B., Schatz, M., Homko, C., and Lemieux, S. (2001). Effects of acute changes of plasma free fatty acids on intramyocellular fat content and insulin resistance in healthy subjects. *Diabetes* 50, 1612–1617.

Bruce, C.R., Hamley, S., Ang, T., Howlett, K.F., Shaw, C.S., and Kowalski, G.M. (2021). Translating glucose tolerance data from mice to humans: Insights from stable isotope labelled glucose tolerance tests. *Mol Metab* 53, 101281.

DeFronzo, R.A., and Tripathy, D. (2009). Skeletal muscle insulin resistance is the primary defect in type 2 diabetes. *Diabetes Care* 32 *Suppl 2*, S157–S163.

Del Prato, S., Leonetti, F., Simonson, D.C., Sheehan, P., Matsuda, M., and DeFronzo, R.A. (1994). Effect of sustained physiologic hyperinsulinaemia and hyperglycaemia on insulin secretion and insulin sensitivity in man. *Diabetologia* 37, 1025–1035.

Demichev, V., Messner, C.B., Vernardis, S.I., Lilley, K.S., and Ralser, M. (2019). DIA-NN: neural networks and interference correction enable deep proteome coverage in high throughput. *Nat. Methods* 17, 41–44.

Fueger, P.T., Lee-Young, R.S., Shearer, J., Bracy, D.P., Heikkinen, S., Laakso, M., Rottman, J.N., and Wasserman, D.H. (2007). Phosphorylation barriers to skeletal and cardiac muscle glucose uptakes in high-fat fed mice: studies in mice with a 50% reduction of hexokinase II. *Diabetes* 56, 2476–2484.

Gancheva, S., Jelenik, T., Álvarez-Hernández, E., and Roden, M. (2018). Interorgan Metabolic Crosstalk in Human Insulin Resistance. *Physiol. Rev.* 98, 1371–1415.

Gareus, R., Di Nardo, A., Rybin, V., and Witke, W. (2006). Mouse profilin 2 regulates endocytosis and competes with SH3 ligand binding to dynamin 1. *J. Biol. Chem.* 281, 2803–2811.

Gaster, M., Staehr, P., Beck-Nielsen, H., Schrøder, H.D., and Handberg, A. (2001). GLUT4 is reduced in slow muscle fibers of type 2 diabetic patients: is insulin resistance in type 2 diabetes a slow, type 1 fiber disease? *Diabetes* 50, 1324–1329.

Guerrero, N., Bunout, D., Hirsch, S., Barrera, G., Leiva, L., Henríquez, S., and De la Maza, M.P. (2016). Premature loss of muscle mass and function in type 2 diabetes. *Diabetes Res. Clin. Pract.* 117, 32–38.

Guillet, C., and Boirie, Y. (2005). Insulin resistance: a contributing factor to age-related muscle mass loss? *Diabetes Metab.* 31 *Spec No 2*, S20–S25.

Hadfield, J.D., and Others (2010). MCMC methods for multi-response generalized linear mixed models: the MCMCglmm R package. *J. Stat. Softw.* 33, 1–22.

Hammarstedt, A., Graham, T.E., and Kahn, B.B. (2012). Adipose tissue dysregulation and reduced insulin sensitivity in non-obese individuals with enlarged abdominal adipose cells. *Diabetol. Metab. Syndr.* 4, 42.

Hanley, A.J.G., Williams, K., Stern, M.P., and Haffner, S.M. (2002). Homeostasis model assessment of insulin resistance in relation to the incidence of cardiovascular disease: the San Antonio Heart Study. *Diabetes Care* 25, 1177–1184.

Ikemoto, S., Thompson, K.S., Takahashi, M., Itakura, H., Lane, M.D., and Ezaki, O. (1995). High fat diet-induced hyperglycemia: prevention by low level expression of a glucose transporter (GLUT4) minigene in transgenic mice. *Proc. Natl. Acad. Sci. U. S. A.* 92, 3096–3099.

Indrakusuma, I., Sell, H., and Eckel, J. (2015). Novel Mediators of Adipose Tissue and Muscle Crosstalk. *Curr. Obes. Rep.* 4, 411–417.

Iozzo, P., Pratipanawatr, T., Pijl, H., Vogt, C., Kumar, V., Pipek, R., Matsuda, M., Mandarino, L.J., Cusi, K.J., and DeFronzo, R.A. (2001). Physiological hyperinsulinemia impairs insulin-stimulated glycogen synthase activity and glycogen synthesis. *Am. J. Physiol. Endocrinol. Metab.* 280, E712–E719.

Ishikura, S., Bilan, P.J., and Klip, A. (2007). Rabs 8A and 14 are targets of the insulin-regulated Rab-GAP AS160 regulating GLUT4 traffic in muscle cells. *Biochem. Biophys. Res. Commun.* 353, 1074–1079.

James, D.E., Strube, M., and Mueckler, M. (1989). Molecular cloning and characterization of an insulin-regulatable glucose transporter. *Nature* 338, 83–87.

James, D.E., Stöckli, J., and Birnbaum, M.J. (2021). The aetiology and molecular landscape of insulin resistance. *Nat. Rev. Mol. Cell Biol.*

Jeong, S., and Yoon, M. (2009). Fenofibrate inhibits adipocyte hypertrophy and insulin resistance by activating adipose PPAR α in high fat diet-induced obese mice. *Exp. Mol. Med.* 41, 397–405.

Jo, J., Gavrilova, O., Pack, S., Jou, W., Mullen, S., Sumner, A.E., Cushman, S.W., and Perival, V. (2009). Hypertrophy and/or Hyperplasia: Dynamics of Adipose Tissue Growth. *PLoS Comput. Biol.* 5, e1000324.

Karp, N.A., Mason, J., Beaudet, A.L., Benjamini, Y., Bower, L., Braun, R.E., Brown, S.D.M., Chesler, E.J., Dickinson, M.E., Flenniken, A.M., et al. (2017). Prevalence of sexual dimorphism in mammalian phenotypic traits. *Nat. Commun.* 8, 15475.

Kim, J.I., Huh, J.Y., Sohn, J.H., Choe, S.S., Lee, Y.S., Lim, C.Y., Jo, A., Park, S.B., Han, W., and Kim, J.B. (2015). Lipid-overloaded enlarged adipocytes provoke insulin

resistance independent of inflammation. *Mol. Cell. Biol.* 35, 1686–1699.

Kim, J.K., Gavrilova, O., Chen, Y., Reitman, M.L., and Shulman, G.I. (2000). Mechanism of insulin resistance in A-ZIP/F-1 fatless mice. *J. Biol. Chem.* 275, 8456–8460.

Kolterman, O.G., Insel, J., Saekow, M., and Olefsky, J.M. (1980). Mechanisms of insulin resistance in human obesity: evidence for receptor and postreceptor defects. *J. Clin. Invest.* 65, 1272–1284.

Koopmans, S.J., Ohman, L., Haywood, J.R., Mandarino, L.J., and DeFronzo, R.A. (1997). Seven days of euglycemic hyperinsulinemia induces insulin resistance for glucose metabolism but not hypertension, elevated catecholamine levels, or increased sodium retention in conscious normal rats. *Diabetes* 46, 1572–1578.

Langfelder, P., and Horvath, S. (2008). WGCNA: an R package for weighted correlation network analysis. *BMC Bioinformatics* 9, 559.

Lantier, L., Williams, A.S., Williams, I.M., Guerin, A., Bracy, D.P., Goelzer, M., Foretz, M., Viollet, B., Hughey, C.C., and Wasserman, D.H. (2020). Reciprocity Between Skeletal Muscle AMPK Deletion and Insulin Action in Diet-Induced Obese Mice. *Diabetes* 69, 1636–1649.

Li, V.L., Kim, J.T., and Long, J.Z. (2020). Adipose Tissue Lipokines: Recent Progress and Future Directions. *Diabetes* 69, 2541–2548.

Lillioja, S., Mott, D.M., Spraul, M., Ferraro, R., Foley, J.E., Ravussin, E., Knowler, W.C., Bennett, P.H., and Bogardus, C. (1993). Insulin resistance and insulin secretory dysfunction as precursors of non-insulin-dependent diabetes mellitus. Prospective studies of Pima Indians. *N. Engl. J. Med.* 329, 1988–1992.

Mittelstrass, K., Ried, J.S., Yu, Z., Krumsiek, J., Gieger, C., Prehn, C., Roemisch-Margl, W., Polonikov, A., Peters, A., Theis, F.J., et al. (2011). Discovery of sexual dimorphisms in metabolic and genetic biomarkers. *PLoS Genet.* 7, e1002215.

Montgomery, M.K., Hallahan, N.L., Brown, S.H., Liu, M., Mitchell, T.W., Cooney, G.J., and Turner, N. (2013). Mouse strain-dependent variation in obesity and glucose homeostasis in response to high-fat feeding. *Diabetologia* 56, 1129–1139.

Mootha, V.K., Lindgren, C.M., Eriksson, K.-F., Subramanian, A., Sihag, S., Lehar, J., Puigserver, P., Carlsson, E., Ridderstråle, M., Laurila, E., et al. (2003). PGC-1 α -responsive genes involved in oxidative phosphorylation are coordinately downregulated in human diabetes. *Nat. Genet.* 34, 267–273.

Newgard, C.B., An, J., Bain, J.R., Muehlbauer, M.J., Stevens, R.D., Lien, L.F., Haqq, A.M., Shah, S.H., Arlotto, M., Slentz, C.A., et al. (2009). A branched-chain amino acid-related metabolic signature that differentiates obese and lean humans and contributes to insulin resistance. *Cell Metab.* 9, 311–326.

- Norheim, F., Hasin-Brumshtein, Y., Vergnes, L., Chella Krishnan, K., Pan, C., Seldin, M.M., Hui, S.T., Mehrabian, M., Zhou, Z., Gupta, S., et al. (2019). Gene-by-Sex Interactions in Mitochondrial Functions and Cardio-Metabolic Traits. *Cell Metab.* *29*, 932–949.e4.
- Palsgaard, J., Brøns, C., Friedrichsen, M., Dominguez, H., Jensen, M., Storgaard, H., Spohr, C., Torp-Pedersen, C., Borup, R., De Meyts, P., et al. (2009). Gene expression in skeletal muscle biopsies from people with type 2 diabetes and relatives: differential regulation of insulin signaling pathways. *PLoS One* *4*, e6575.
- Parker, B.L., Calkin, A.C., Seldin, M.M., Keating, M.F., Tarling, E.J., Yang, P., Moody, S.C., Liu, Y., Zerenturk, E.J., Needham, E.J., et al. (2019). An integrative systems genetic analysis of mammalian lipid metabolism. *Nature* *567*, 187–193.
- Parks, B.W., Sallam, T., Mehrabian, M., Psychogios, N., Hui, S.T., Norheim, F., Castellani, L.W., Rau, C.D., Pan, C., Phun, J., et al. (2015). Genetic architecture of insulin resistance in the mouse. *Cell Metab.* *21*, 334–347.
- Perez-Riverol, Y., Csordas, A., Bai, J., Bernal-Llinares, M., Hewapathirana, S., Kundu, D.J., Inuganti, A., Griss, J., Mayer, G., Eisenacher, M., et al. (2019). The PRIDE database and related tools and resources in 2019: improving support for quantification data. *Nucleic Acids Res.* *47*, D442–D450.
- Rappsilber, J., Mann, M., and Ishihama, Y. (2007). Protocol for micro-purification, enrichment, pre-fractionation and storage of peptides for proteomics using StageTips. *Nat. Protoc.* *2*, 1896–1906.
- Ritchie, M.E., Phipson, B., Wu, D., Hu, Y., Law, C.W., Shi, W., and Smyth, G.K. (2015). limma powers differential expression analyses for RNA-sequencing and microarray studies. *Nucleic Acids Res.* *43*, e47.
- Rodeheffer, M.S., Birsoy, K., and Friedman, J.M. (2008). Identification of white adipocyte progenitor cells in vivo. *Cell* *135*, 240–249.
- Roden, M., Price, T.B., Perseghin, G., Petersen, K.F., Rothman, D.L., Cline, G.W., and Shulman, G.I. (1996). Mechanism of free fatty acid-induced insulin resistance in humans. *J. Clin. Invest.* *97*, 2859–2865.
- Salans, L.B., Knittle, J.L., and Hirsch, J. (1968). The role of adipose cell size and adipose tissue insulin sensitivity in the carbohydrate intolerance of human obesity. *J. Clin. Invest.* *47*, 153–165.
- Sears, D.D., Hsiao, G., Hsiao, A., Yu, J.G., Courtney, C.H., Ofrecio, J.M., Chapman, J., and Subramaniam, S. (2009). Mechanisms of human insulin resistance and thiazolidinedione-mediated insulin sensitization. *Proc. Natl. Acad. Sci. U. S. A.* *106*, 18745–18750.
- da Silva Rosa, S.C., Nayak, N., Caymo, A.M., and Gordon, J.W. (2020). Mechanisms of

muscle insulin resistance and the cross-talk with liver and adipose tissue. *Physiol. Rep.* **8**, e14607.

Simoneau, J.-A., and Kelley, D.E. (1997). Altered glycolytic and oxidative capacities of skeletal muscle contribute to insulin resistance in NIDDM. *Journal of Applied Physiology* **83**, 166–171.

Sinasac, D.S., Riordan, J.D., Spiezio, S.H., Yandell, B.S., Croniger, C.M., and Nadeau, J.H. (2016). Genetic control of obesity, glucose homeostasis, dyslipidemia and fatty liver in a mouse model of diet-induced metabolic syndrome. *Int. J. Obes.* **40**, 346–355.

Small, L., Brandon, A.E., Quek, L.-E., Krycer, J.R., James, D.E., Turner, N., and Cooney, G.J. (2018). Acute activation of pyruvate dehydrogenase increases glucose oxidation in muscle without changing glucose uptake. *Am. J. Physiol. Endocrinol. Metab.* **315**, E258–E266.

Stöckli, J., Fisher-Wellman, K.H., Chaudhuri, R., Zeng, X.-Y., Fazakerley, D.J., Meoli, C.C., Thomas, K.C., Hoffman, N.J., Mangiafico, S.P., Xirouchaki, C.E., et al. (2017). Metabolomic analysis of insulin resistance across different mouse strains and diets. *J. Biol. Chem.* **292**, 19135–19145.

Stuart, C.A., McCurry, M.P., Marino, A., South, M.A., Howell, M.E.A., Layne, A.S., Ramsey, M.W., and Stone, M.H. (2013). Slow-twitch fiber proportion in skeletal muscle correlates with insulin responsiveness. *J. Clin. Endocrinol. Metab.* **98**, 2027–2036.

Surwit, R.S., Kuhn, C.M., Cochrane, C., McCubbin, J.A., and Feinglos, M.N. (1988). Diet-induced type II diabetes in C57BL/6J mice. *Diabetes* **37**, 1163–1167.

Tam, V., Patel, N., Turcotte, M., Bossé, Y., Paré, G., and Meyre, D. (2019). Benefits and limitations of genome-wide association studies. *Nat. Rev. Genet.* **20**, 467–484.

Tan, S.-X., Fisher-Wellman, K.H., Fazakerley, D.J., Ng, Y., Pant, H., Li, J., Meoli, C.C., Coster, A.C.F., Stöckli, J., and James, D.E. (2015). Selective insulin resistance in adipocytes. *J. Biol. Chem.* **290**, 11337–11348.

Tanner, L.B., Goglia, A.G., Wei, M.H., Sehgal, T., Parsons, L.R., Park, J.O., White, E., Toettcher, J.E., and Rabinowitz, J.D. (2018). Four Key Steps Control Glycolytic Flux in Mammalian Cells. *Cell Syst* **7**, 49–62.e8.

TeSlaa, T., Bartman, C.R., Jankowski, C.S.R., Zhang, Z., Xu, X., Xing, X., Wang, L., Lu, W., Hui, S., and Rabinowitz, J.D. (2021). The Source of Glycolytic Intermediates in Mammalian Tissues. *Cell Metab.* **33**(2):367-378.e5.

Vander Heiden, M.G., Cantley, L.C., and Thompson, C.B. (2009). Understanding the Warburg effect: the metabolic requirements of cell proliferation. *Science* **324**, 1029–1033.

Virtue, S., and Vidal-Puig, A. (2021). GTTs and ITTs in mice: simple tests, complex

answers. *Nat Metab* 3, 883–886.

Vishvanath, L., and Gupta, R.K. (2019). Contribution of adipogenesis to healthy adipose tissue expansion in obesity. *J. Clin. Invest.* 129, 4022–4031.

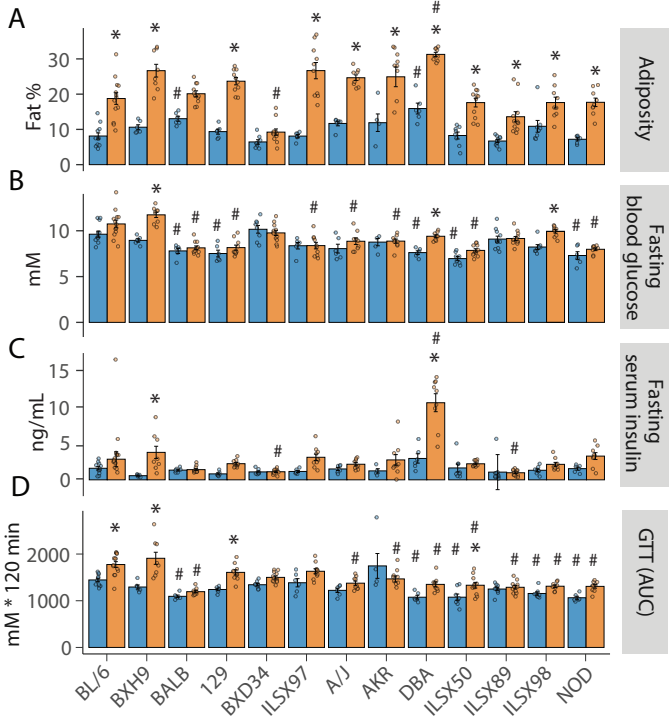
White, P.J., Lapworth, A.L., An, J., Wang, L., McGarrah, R.W., Stevens, R.D., Ilkayeva, O., George, T., Muehlbauer, M.J., Bain, J.R., et al. (2016). Branched-chain amino acid restriction in Zucker-fatty rats improves muscle insulin sensitivity by enhancing efficiency of fatty acid oxidation and acyl-glycine export. *Mol Metab* 5, 538–551.

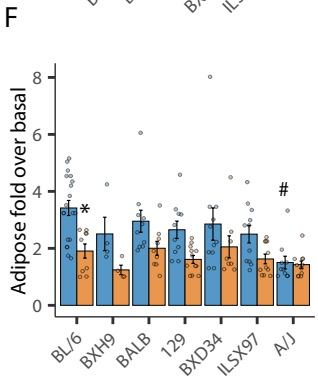
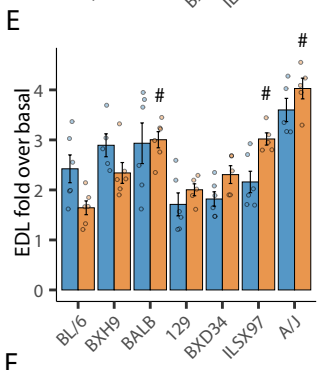
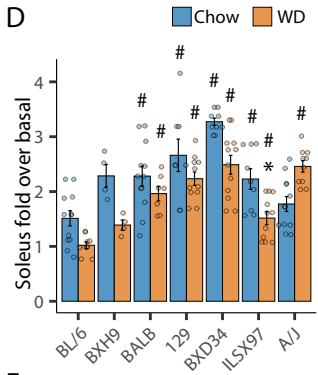
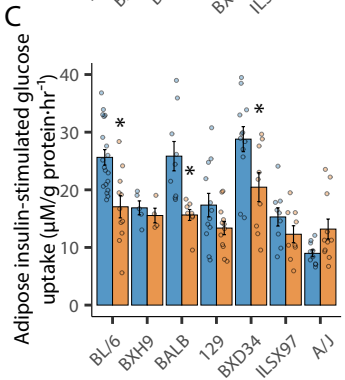
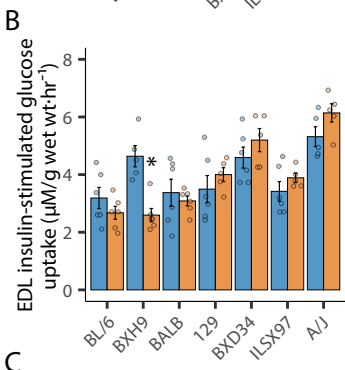
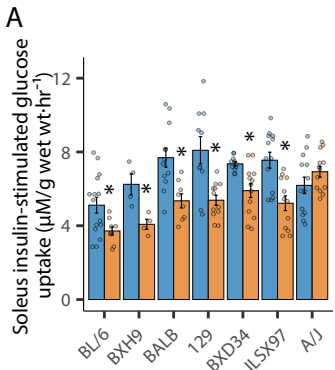
Williams, E.G., Wu, Y., Jha, P., Dubuis, S., Blattmann, P., Argmann, C.A., Houten, S.M., Amariuta, T., Wolski, W., Zamboni, N., et al. (2016). Systems proteomics of liver mitochondria function. *Science* 352, aad0189.

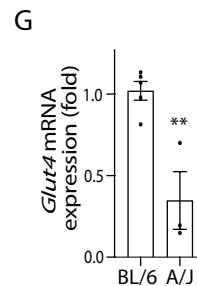
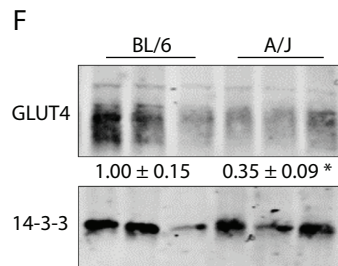
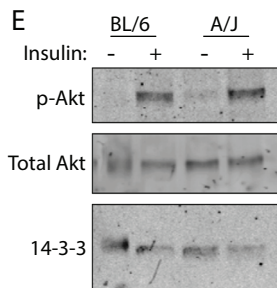
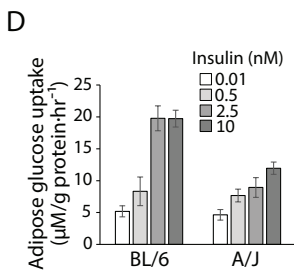
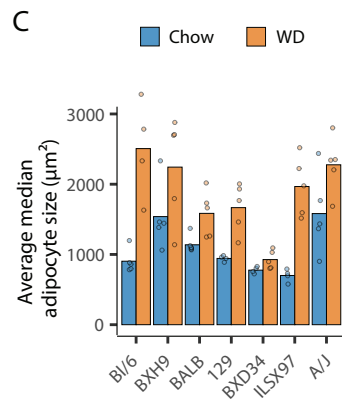
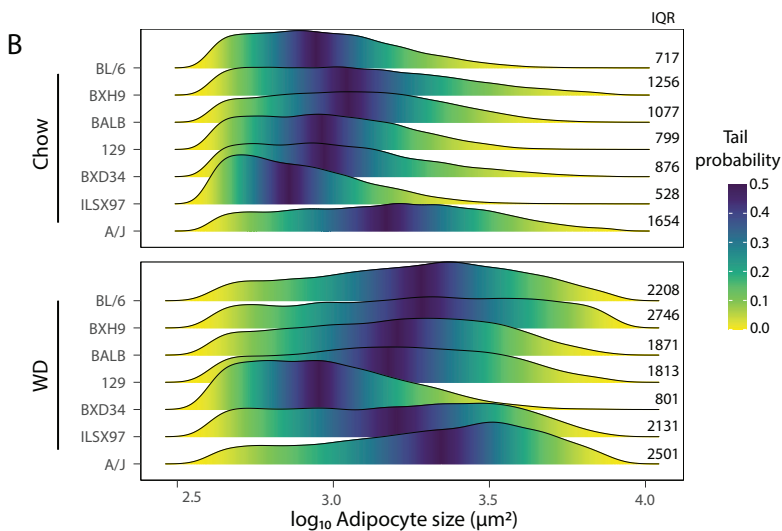
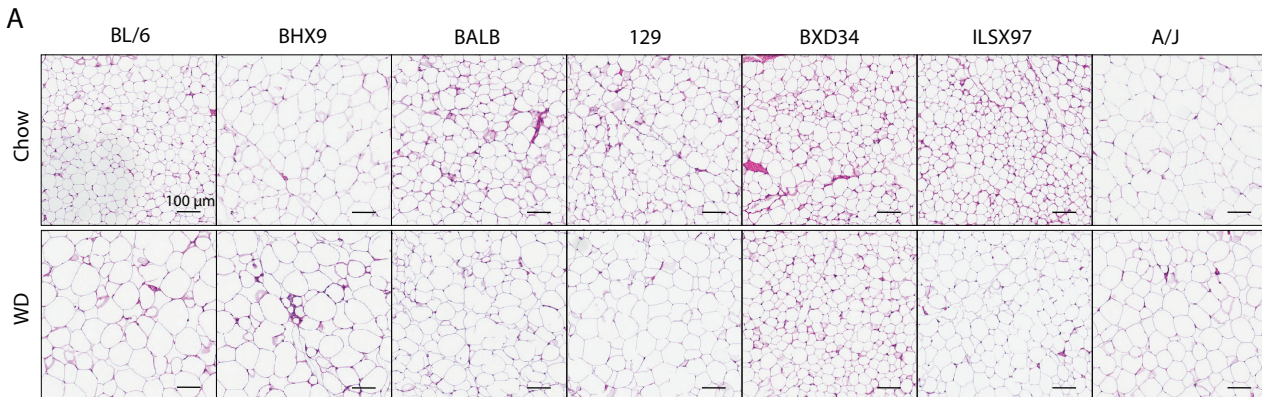
Xiang, C., Zhang, Y., Chen, Q., Sun, A., Peng, Y., Zhang, G., Zhou, D., Xie, Y., Hou, X., Zheng, F., et al. (2021). Increased glycolysis in skeletal muscle coordinates with adipose tissue in systemic metabolic homeostasis. *J. Cell. Mol. Med.* 25, 7840–7854.

Zhang, B., Kirov, S., and Snoddy, J. (2005). WebGestalt: an integrated system for exploring gene sets in various biological contexts. *Nucleic Acids Res.* 33, W741–W748.

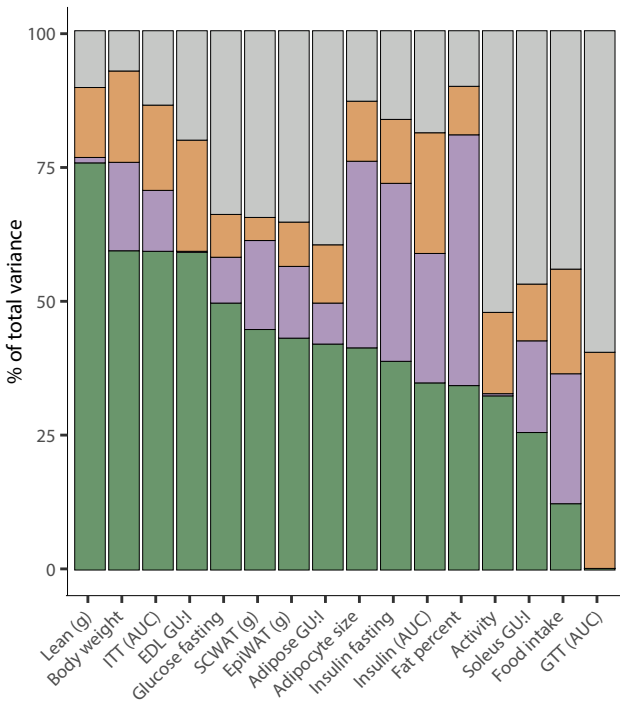
Diet ■ Chow ■ WD



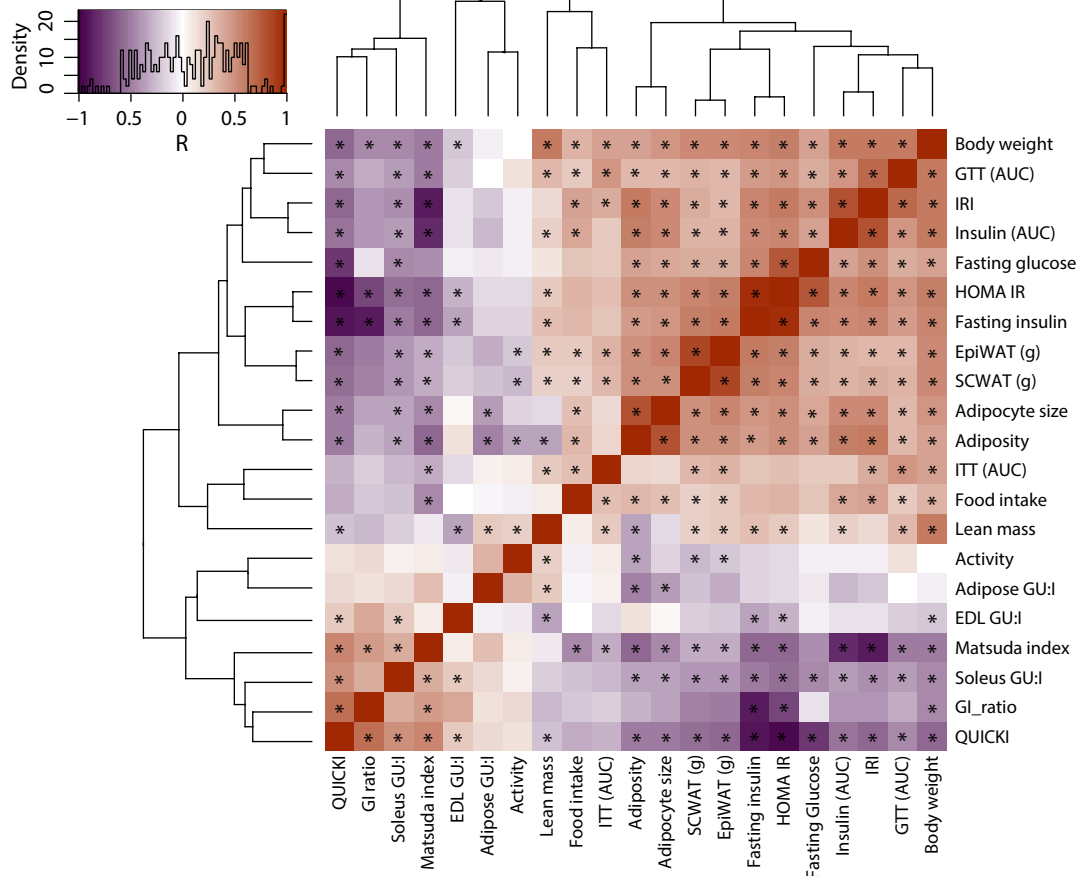




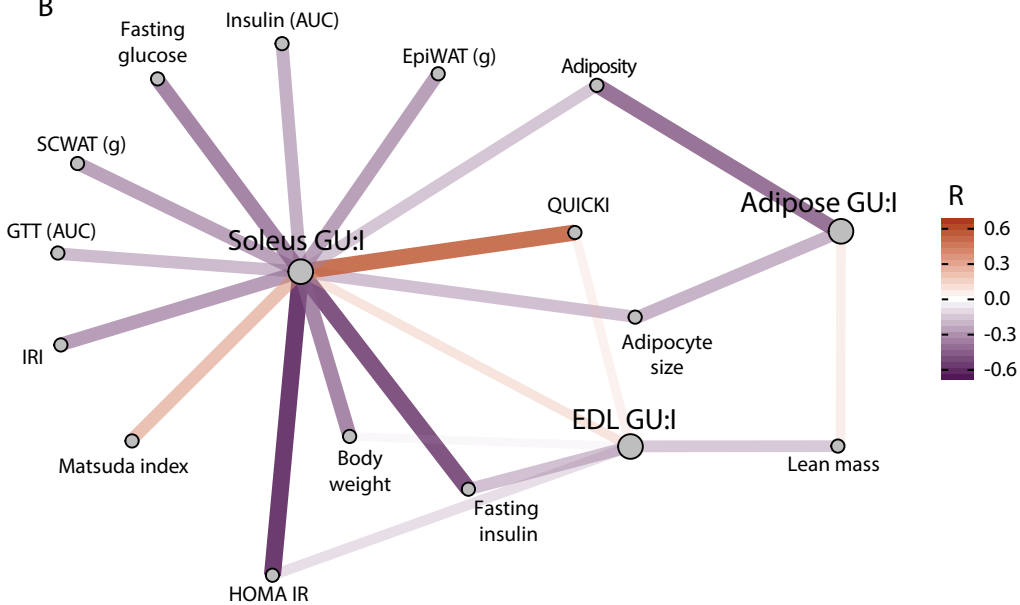
Variance source ■ Strain (H2) ■ Diet ■ Strain x Diet ■ Residual



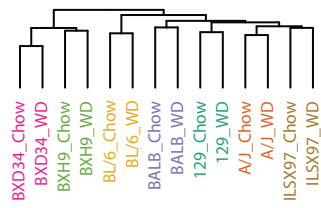
A



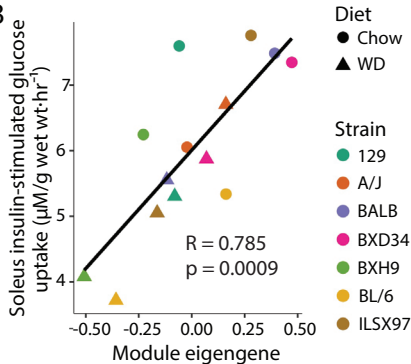
B



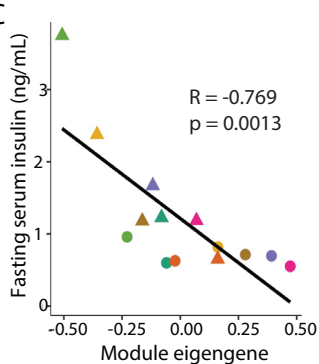
A



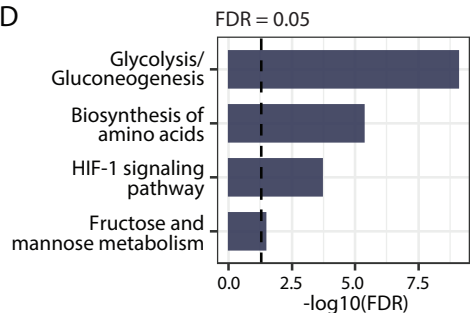
B



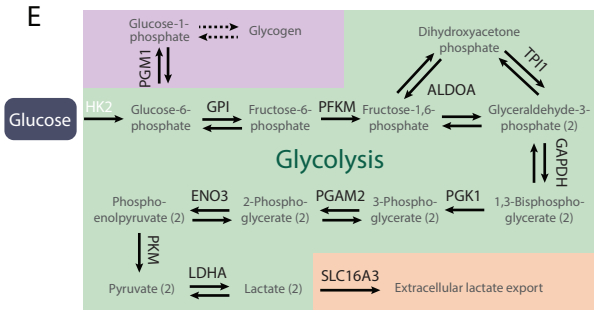
C



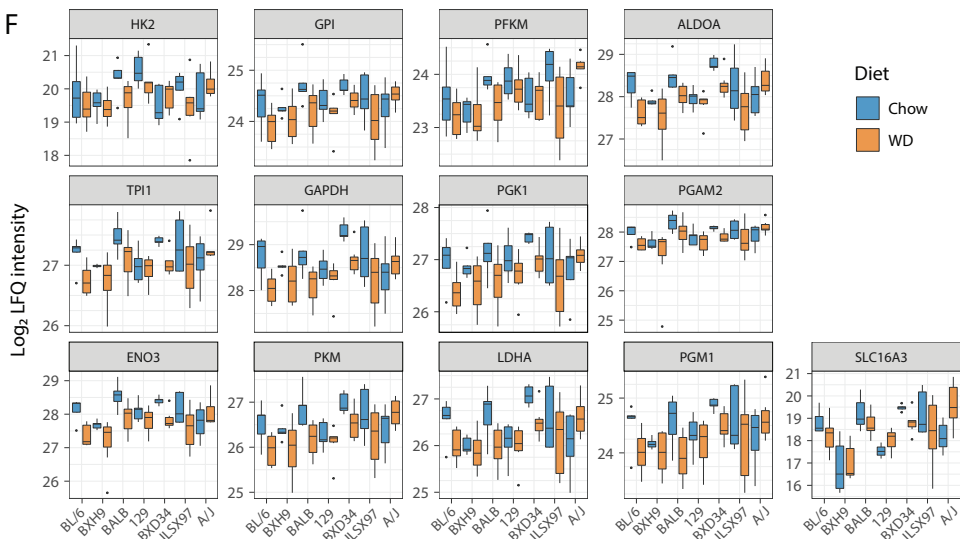
D



E



F



SUPPLEMENTAL MATERIALS

Nelson et al. "Systems level analysis of insulin action reveals insights into whole body metabolism and insulin action in muscle and adipose tissue."

SUPPLEMENTAL FIGURES AND FIGURE LEGENDS

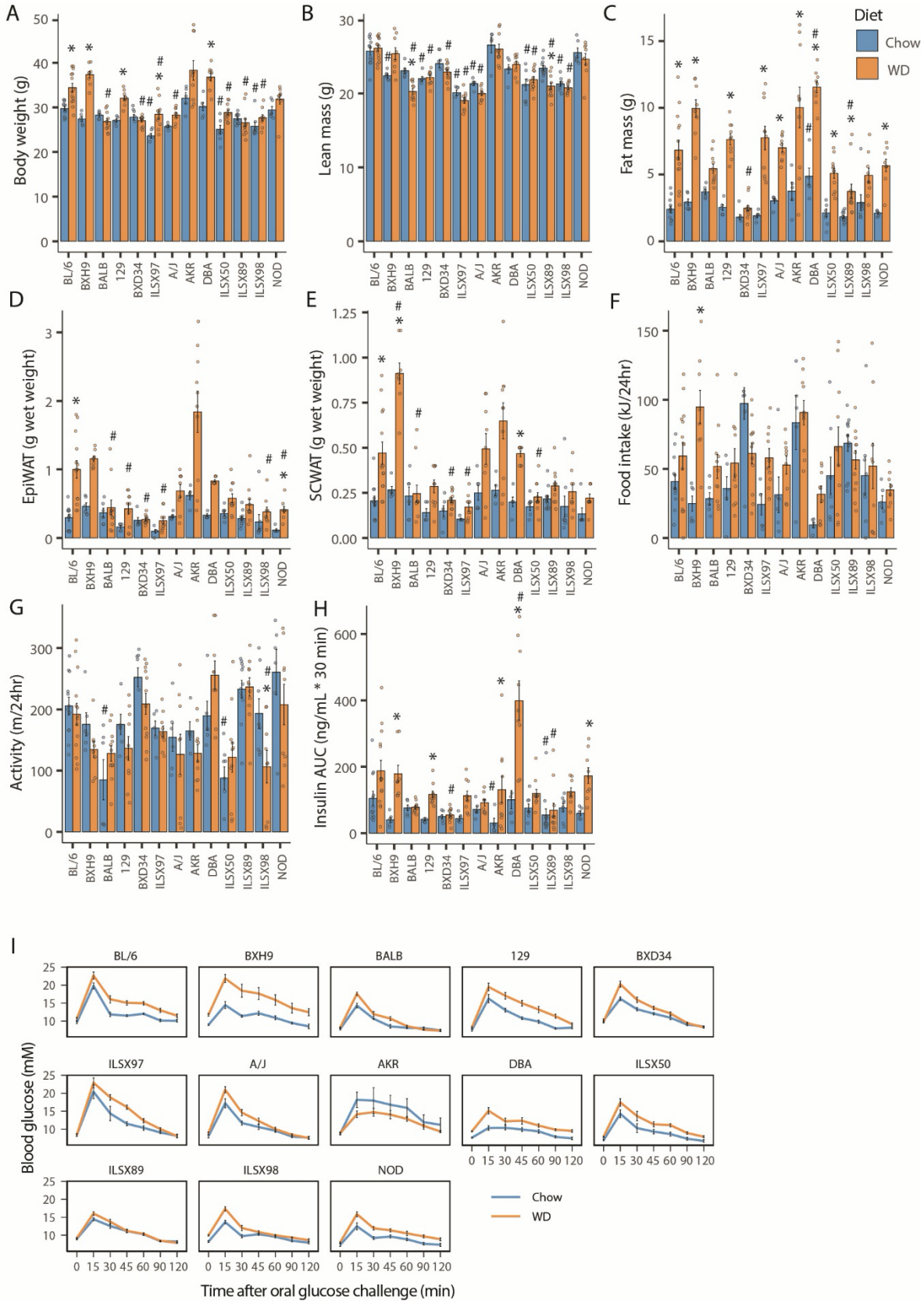


FIGURE S1. Metabolic traits across thirteen mouse strains and two diets (Related to FIG 1). In thirteen mouse strains fed chow or six to eight weeks of WD feeding, **(A)** total body weight, **(B)** lean mass, **(C)** fat mass, weights of **(D)** epididymal white adipose tissue (EpiWAT) and **(E)** subcutaneous white adipose tissue (SCWAT). 24-h sampling of **(F)** food intake and **(G)** ambient activity. **(H)** Blood insulin concentration AUC over the first 30 minutes of an oral glucose tolerance test (oGTT). **(I)** Blood glucose concentrations over time over 120 minutes of an oGTT. Error bars represent means \pm SEM. Significant differences between group means were tested on log-transformed data by a two-way ANOVA, followed by a Tukey's post hoc test. * indicate a significant difference between chow and WD within a strain, # indicate a significant difference between BL/6 and another strain within the same diet; $p < 0.05$.

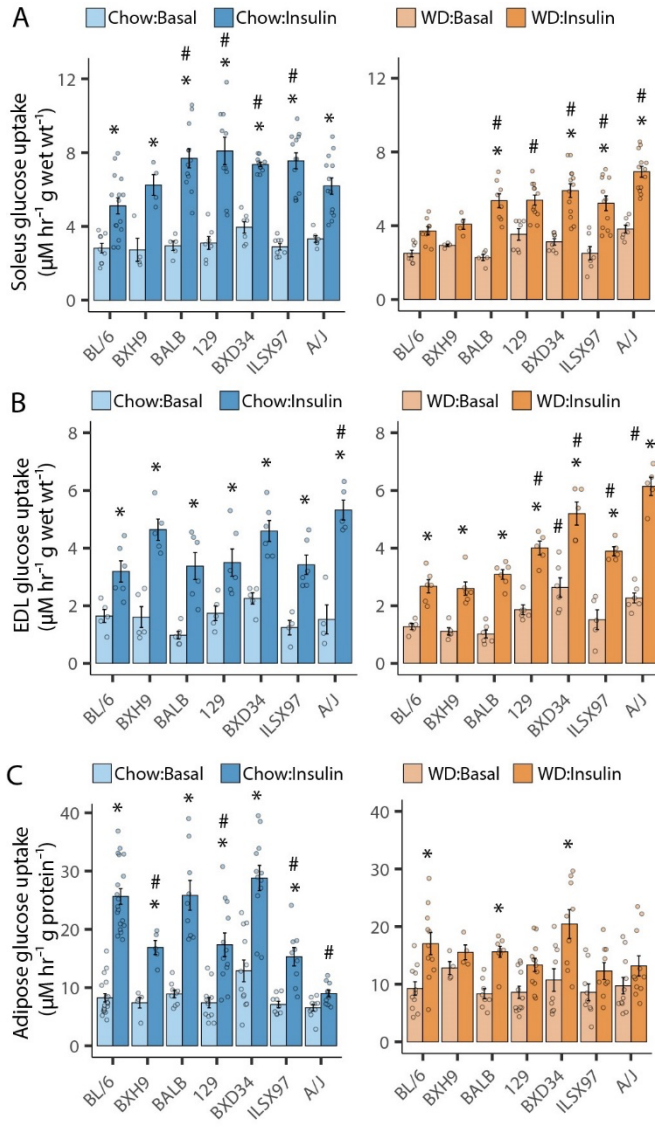


FIGURE S2. Muscle and adipose tissue insulin responsiveness (related to FIG 2). Insulin-stimulated (10 nM) or basal (0 nM) *ex vivo* glucose uptake into intact **(A)** soleus and **(B)** EDL or **(C)** minced epididymal white adipose tissue excised from seven selected mouse strains fed chow or eight weeks of WD. These insulin-stimulated data are repeated in Fig. 2 for comparison of insulin-stimulated chow versus WD values. Error bars represent means \pm SEM. Significant differences between group means were tested on log-transformed data by a two-way ANOVA, followed by a Tukey's post hoc test. * indicate a significant difference between basal and insulin-stimulated within a strain, # indicate a significant difference between BL/6 and another strain within the same diet; $p < 0.05$.

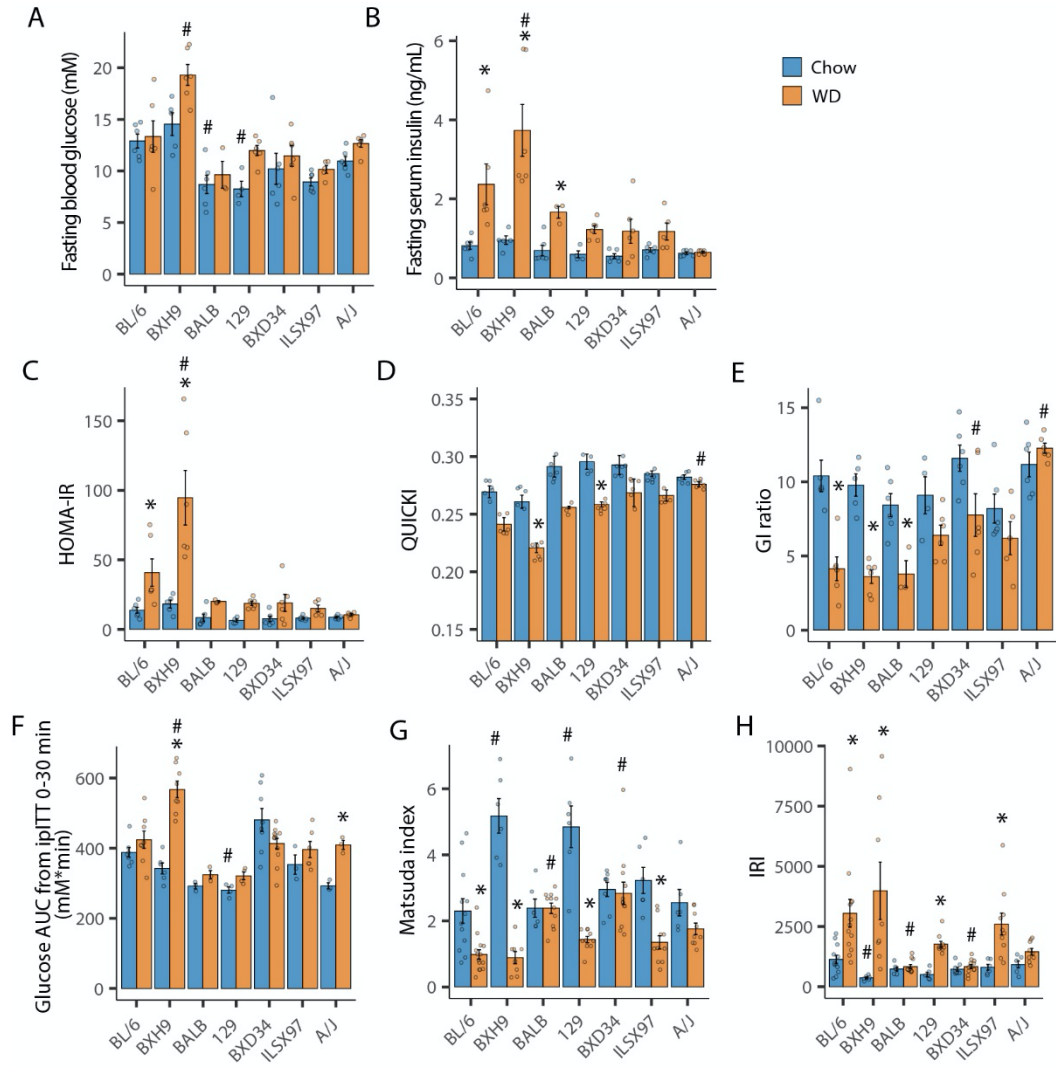


FIGURE S3. Glucose homeostasis (related to FIG 5). Six-hour fasting **(A)** blood glucose and **(B)** serum insulin in mice from the seven selected strains fed chow or seven weeks of WD. Measures calculated from these fasting glucose and fasting insulin values: **(C)** HOMA-IR, **(D)** QUICKI and **(E)** GI ratio. Blood glucose concentration area under the curve (AUC) over **(F)** 30 minutes of an intraperitoneal insulin tolerance test (ipITT). **(G)** Matsuda index calculated from fasting blood glucose and insulin values and the average glucose and insulin values during an oGTT. **(H)** IRI calculated from fasting insulin and oGTT AUC (Fig. S1H). Bars represent group means and points represent individual mice. Error bars represent means \pm SEM. Significant differences between group means were tested on log-transformed data by a two-way ANOVA, followed by a Tukey's post hoc test. * indicate a significant difference between chow and WD within a strain, # indicate a significant difference between BL/6 and another strain within the same diet; $p < 0.05$.

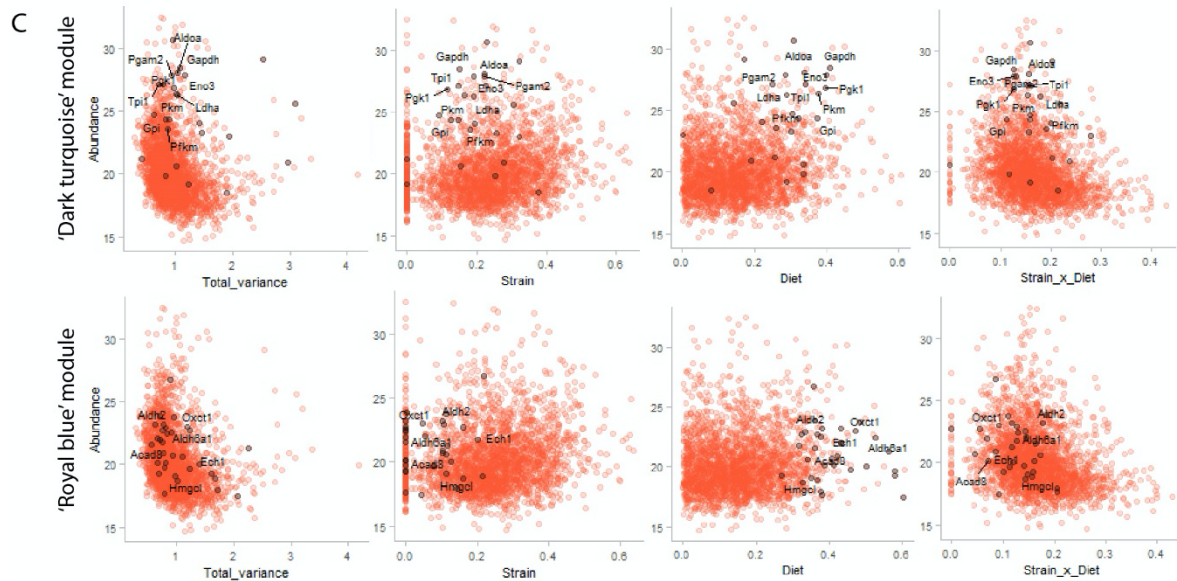
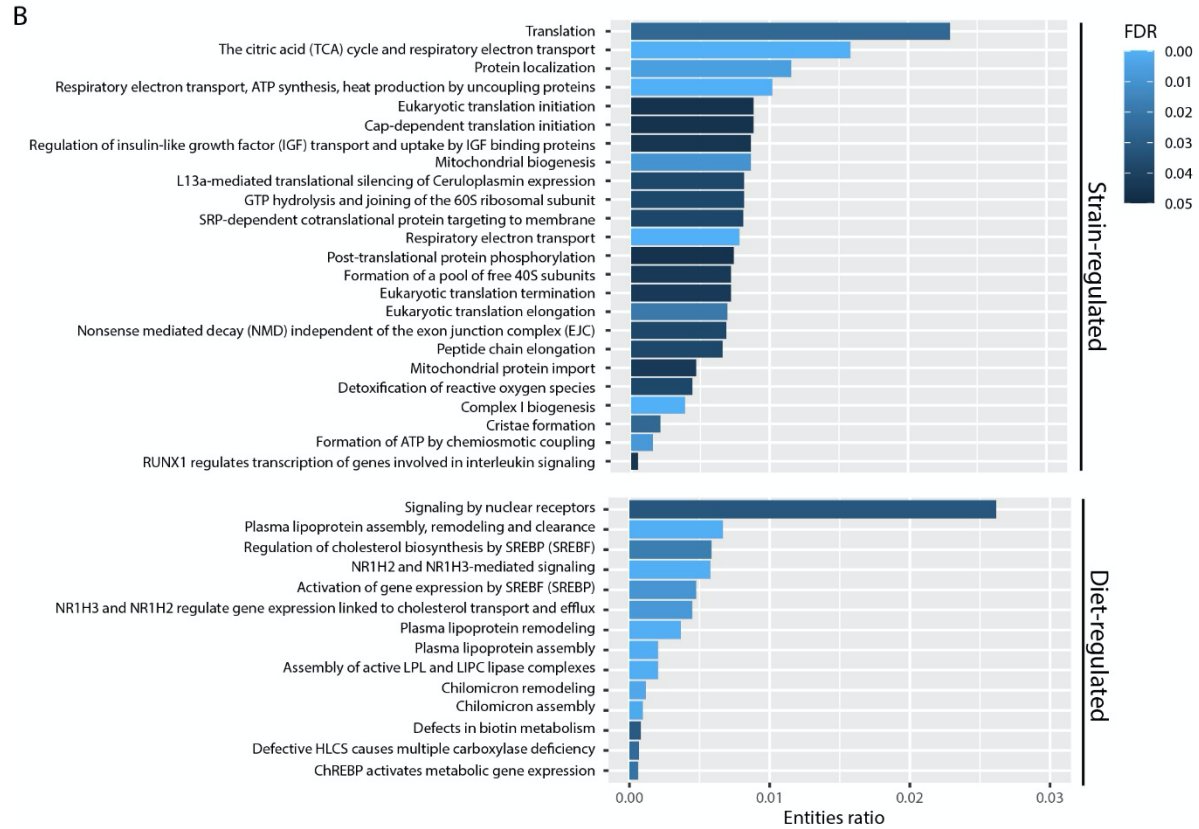
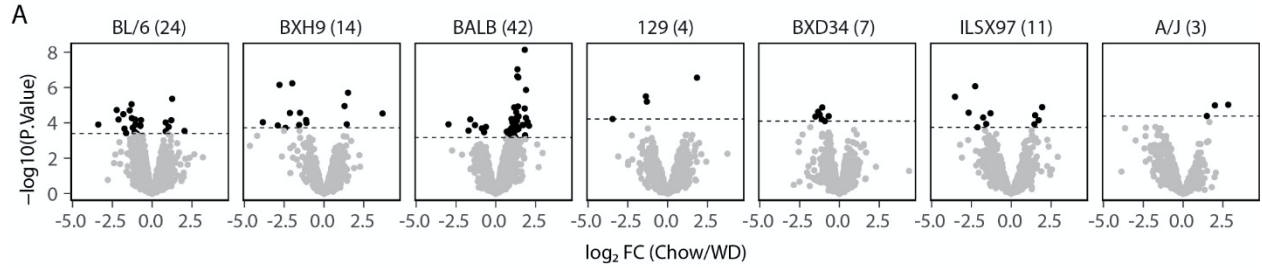


FIGURE S4. Variance partitioning of the soleus proteome (related to FIG 7). **(A)** Volcano plots comparing the chow vs WD soleus proteome for each strain. Significantly regulated proteins are represented by black dots. The number in parenthesis indicates the number of significantly regulated protein within each strain. For **B-C**, linear mixed models were used to partition variance in expression of each protein in the soleus proteomics dataset by total, strain, diet, strain-by-diet or residual variance. **(B)** Pathway overrepresentation of the top 100 strain- or diet-regulated proteins. **(C)** For all proteins in the dataset, each of the variance sources was plotted against mean protein abundance (\log_2 LFQ intensity) (orange dots). Each protein contained in the respective modules is represented by gray dots. For the 'dark turquoise' module, proteins belonging to the canonical glycolytic pathway (Fig. 6E) are labeled. For the 'royal blue' module, proteins involved in BCAA, aldehyde and ketone metabolism are labeled.

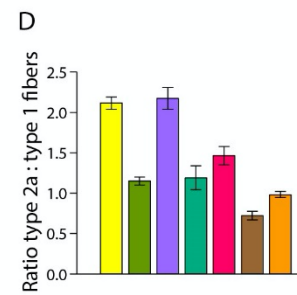
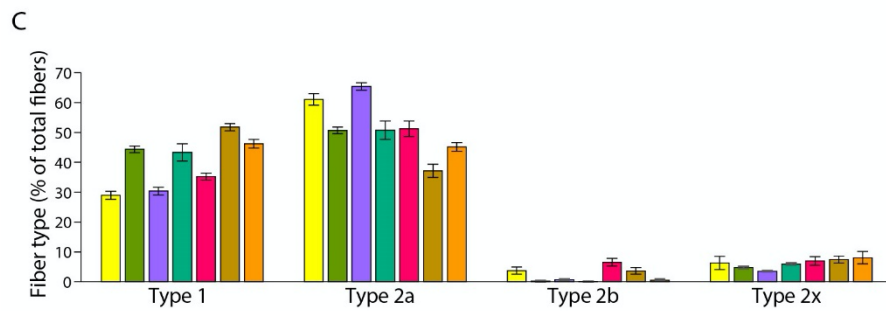
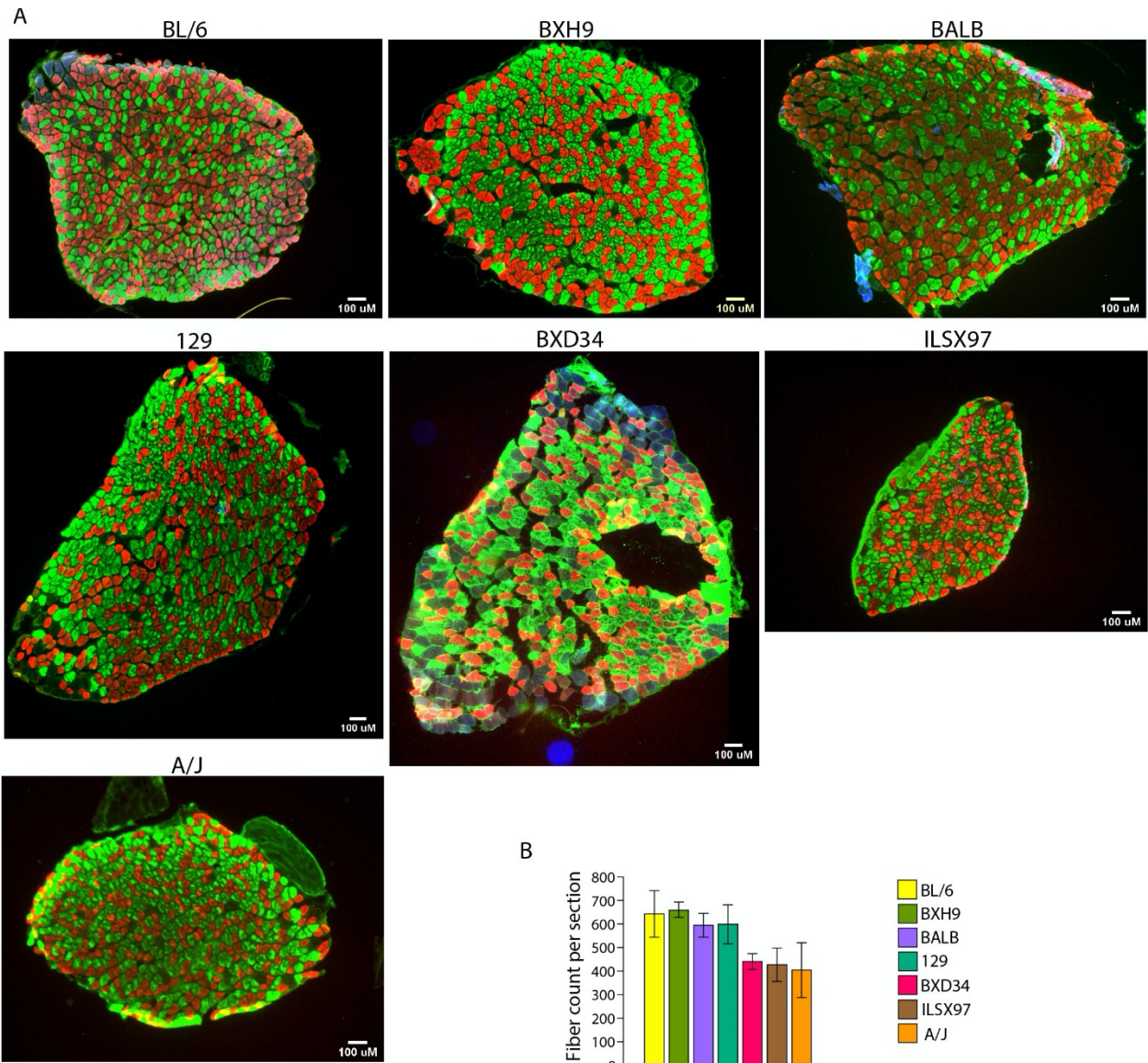


FIGURE S5. Soleus muscle fiber typing (related to FIG 7). Soleus muscles of chow-fed mice were cross-sectioned and the fibers were stained green (type 1), red (type 2a), blue (type 2b), or remained unstained (type 2x). **(A)** Representative images and quantification of **(B)** total fibers per cross sectional area, **(C)** each fiber type as a percentage of total fibers and **(D)** the ratio of type 2a to type 1 fibers. Bars represent group means. Error bars represent means \pm SEM (n=3-7).

SUPPLEMENTAL TABLE

Supplemental Table 1 (related to FIG 7). Data independent analysis windows for mass spectrometry method.

DIA window	Min	Max	m/z centre	Isolation window (+/-)
1	350	394	372	22
2	393	424	408.5	31
3	423	452	437.5	29
4	451	478	464.5	27
5	477	504	490.5	27
6	503	529	516	26
7	528	555	541.5	27
8	554	581	567.5	27
9	580	608	594	28
10	607	635	621	28
11	634	663	648.5	29
12	662	693	677.5	31
13	692	725	708.5	33
14	724	759	741.5	35
15	758	798	778	40
16	797	841	819	44
17	840	892	866	52
18	891	959	925	68
19	958	1062	1010	104
20	1061	1650	1355.5	589